Charge radii and electromagnetic moments of $^{195-211}$At

J. G. Cubiss,[1,*] A. E. Barzakh,[2] M. D. Seliverstov,[1,2] A. N. Andreyev,[1,3,4,5] B. Andel,[6] S. Antalic,[6] P. Ascher,[7,†] D. Atanasov,[7,‡] D. Beck,[8] J. Bieroń,[9] K. Blaum,[7] Ch. Borgmann,[7] M. Breitenfeldt,[10] L. Capponi,[4] T. E. Cocolios,[5,10,11] T. Day Goodacre,[5,11,§] X. Derkx,[4,12] H. De Witte,[10] J. Elseviers,[10] D. V. Fedorov,[2] V. N. Fedosseev,[5] S. Fritzsche,[13,14] L. P. Gaffney,[10] S. George,[7] L. Ghys,[10,15] F. P. Heßberger,[16,17] M. Huyse,[10] N. Imai,[5,18] Z. Kalaninová,[6,19] D. Kisler,[7] U. Köster,[20] M. Kowalska,[5] S. Kreim,[5,7] J. F. W. Lane,[4] V. Liberati,[4] D. Lunney,[21] K. M. Lynch,[5,11] V. Manea,[5,21] B. A. Marsh,[5] S. Mitsuoka,[3] P. L. Molkanov,[2] Y. Nagame,[3] D. Neidherr,[8] K. Nishio,[3] S. Ota,[3] D. Pauwels,[15] L. Popescu,[15] D. Radulov,[10] E. Rapisarda,[5] J. P. Revill,[22] M. Rosenbusch,[23,‖] R. E. Rossel,[5,24] S. Rothe,[5,24] K. Sandhu,[4] L. Schweikhard,[23] S. Sels,[10] V. L. Truesdale,[1] C. Van Beveren,[10] P. Van den Bergh,[10] Y. Wakabayashi,[3] P. Van Duppen,[10] K. D. A. Wendt,[24] F. Wienholtz,[5,23] B. W. Whitmore,[1] G. L. Wilson,[1] R. N. Wolf,[7,23,¶] and K. Zuber[25]

[1]*Department of Physics, University of York, York, YO10 5DD, United Kingdom*
[2]*Petersburg Nuclear Physics Institute, NRC Kurchatov Institute, 188300 Gatchina, Russia*
[3]*Advanced Science Research Center, Japan Atomic Energy Agency, Tokai-Mura, Naka-gun, Ibaraki 319-1195, Japan*
[4]*School of Engineering, University of the West of Scotland, Paisley PA1 2BE, United Kingdom*
[5]*CERN, CH-1211 Geneva 23, Switzerland*
[6]*Department of Nuclear Physics and Biophysics, Comenius University in Bratislava, 84248 Bratislava, Slovakia*
[7]*Max-Planck-Institut für Kernphysik, 69117 Heidelberg, Germany*
[8]*GSI Helmholtzzentrum für Schwerionenforschung GmbH, 64291 Darmstadt, Germany*
[9]*Instytut Fizyki imienia Mariana Smoluchowskiego, Uniwersytet Jagielloński, ul. prof. Stanisława Łojasiewicza 11, Kraków, Poland*
[10]*KU Leuven, Instituut voor Kern- en Stralingsfysica, B-3001 Leuven, Belgium*
[11]*School of Physics and Astronomy, The University of Manchester, Manchester M13 9PL, United Kingdom*
[12]*LPC, ENSICAEN, Université de Caen Basse Normandie, CNRS/IN2P3-ENSI, Caen F-14050, France*
[13]*Helmholtz-Institut Jena, Fröbelstieg 3, D-07743 Jena, Germany*
[14]*Theoretisch-Physikalisches Institut, Friedrich-Schiller-Universität Jena, Max-Wien-Platz 1, D-07743 Jena, Germany*
[15]*Belgian Nuclear Research Center SCK CEN, Boeretang 200, B-2400 Mol, Belgium*
[16]*Gesellschaft für Schwerionenforschung, Planckstrasse 1, D-64291 Darmstadt, Germany*
[17]*Helmholtz Institut Mainz, 55099 Mainz, Germany*
[18]*High Energy Accelerator Research Organisation (KEK), Oho 1-1, Tsukuba, Ibaraki 305-0801, Japan*
[19]*Laboratory of Nuclear Problems, JINR, 141980 Dubna, Russia*
[20]*Institut Laue Langevin, 71 avenue des Martyrs, F-38042 Grenoble Cedex 9, France*
[21]*CSNSM-IN2P3-CNRS, Université Paris-Sud, 91406 Orsay, France*
[22]*Oliver Lodge Laboratory, University of Liverpool, Liverpool, L69 7ZE, United Kingdom*
[23]*Ernst-Moritz-Arndt-Universität, Institut für Physik, 17487 Greifswald, Germany*
[24]*Institut für Physik, Johannes Gutenberg-Universität, D-55099 Mainz, Germany*
[25]*Technische Universität Dresden, 01069 Dresden, Germany*

(Received 7 December 2017; published 29 May 2018)

Hyperfine-structure parameters and isotope shifts of $^{195-211}$At have been measured for the first time at CERN-ISOLDE, using the in-source resonance-ionization spectroscopy method. The hyperfine structures of isotopes were recorded using a triad of experimental techniques for monitoring the photo-ion current. The Multi-Reflection Time-of-Flight Mass Spectrometer, in connection with a high-resolution electron multiplier, was used as an ion-counting setup for isotopes that either were affected by strong isobaric contamination or possessed a long half-life; the ISOLDE Faraday cups were used for cases with high-intensity beams; and the Windmill decay station was used for short-lived, predominantly α-decaying nuclei. The electromagnetic moments and changes in the mean-square

[*]james.cubiss@york.ac.uk
[†]Present address: Centre d'Etudes Nucléaires de Bordeaux-Gradignan, 19 Chemin du Solarium, CS 10120, F-33175 Gradignan, France.
[‡]Present address: Technische Universität Dresden, 01069 Dresden, Germany.
[§]Present address: TRIUMF, 4004 Wesbrook Mall, Vancouver BC V6T 2A3, Canada.
[‖]Present address: RIKEN Nishina Center for Accelerator-Based Science, 351-0198 Saitama, Japan.
[¶]Present address: ARC Centre of Excellence for Engineered Quantum Systems, The University of Sydney, NSW 2006, Australia.

charge radii of the astatine nuclei have been extracted from the measured hyperfine-structure constants and isotope shifts. This was only made possible by dedicated state-of-the-art large-scale atomic computations of the electronic factors and the specific mass shift of atomic transitions in astatine that are needed for these extractions. By comparison with systematics, it was possible to assess the reliability of the results of these calculations and their ascribed uncertainties. A strong deviation in the ground-state mean-square charge radii of the lightest astatine isotopes, from the trend of the (spherical) lead isotopes, is interpreted as the result of an onset of deformation. This behavior bears a resemblance to the deviation observed in the isotonic polonium isotopes. Cases for shape coexistence have been identified in ^{197,199}At, for which a significant difference in the charge radii for ground $(9/2^-)$ and isomeric $(1/2^+)$ states has been observed.

DOI: 10.1103/PhysRevC.97.054327

I. INTRODUCTION

Laser spectroscopy provides a powerful tool for model-independent studies of shape coexistence and shape evolution phenomena in nuclei. In particular, measurements of changes in the mean-square charge radius ($\delta\langle r^2\rangle$), magnetic dipole (μ) and spectroscopic quadrupole (Q_S) moments provide insight into the underlying nuclear structure and the collective and single-particle properties of nuclei.

Until recently, the application of resonance photoionization methods for the investigation of astatine isotopes was not possible. This was due to the lack of information on the atomic level structure in astatine atoms, as a result of the longest-lived isotopes of astatine (e.g., $^{207-211}$At) having half-lives of only a few hours. Recent studies at CERN and TRIUMF [1,2] determined the astatine ionization potential and identified a number of excited atomic states (in addition to the two low-lying levels known since the 1960s [3]). Several suitable ionization schemes were found, which provide an effective way for producing isotopes of astatine online, thereby enabling isotope shift (IS) and hyperfine structure (hfs) measurements by resonance ionization spectroscopy to be performed.

It should be stressed, however, that due to the absence of a stable or very long-lived astatine isotope, it is impossible to apply standard semiempirical or calibration procedures to determine the atomic factors needed for the extraction of the nuclear parameters from the hfs constants and IS values [4]. Therefore, large-scale atomic calculations are the only way to convert atomic observables to the nuclear parameters. Such dedicated calculations have been performed in the framework of this study. The assessment of their reliability and the uncertainties ascribed to them was one of the aims of the work presented here.

To cover the whole lifetime range of the At isotopes (from 5 h to 30 ms), the multi-reflection time-of-flight mass spectrometer (MR-TOF MS) [5] was used for the first time, in addition to the Windmill and Faraday cup methods that have previously been used for photo-ion current monitoring [6,7]. The MR-TOF MS allowed access to isotopes that could not be investigated with the other methods, due to too long a half-life or unfavorable α-decay branching ratios, many of which were affected by an otherwise prohibitive amount of isobaric contamination. This combination of measurement techniques substantially widens the range of applicability of the in-source resonance ionization method, making possible the study of isotopes that would be otherwise inaccessible.

Neutron-deficient astatine ($Z = 85$) nuclei demonstrate a rich variety of shape coexistence and shape evolution phenomena. The ground states of the odd-A astatine isotopes are usually associated with the occupation of the $\pi h_{9/2}$ orbital [π(3p-0h) configuration], which leads to a spin-parity assignment of $I^\pi_{gs} = 9/2^-$ in the vicinity of the $N = 126$ shell closure. In the lighter astatine isotopes ^{197,199,201,203}At, the $9/2^-$ ground states coexist with low-lying $1/2^+$ isomers. Furthermore, the ground states in ^{191,193,195}At are seen to possess spins and parities of $I^\pi_{gs} = 1/2^+$ [8,9]. These $1/2^+$ states in the odd-A astatine isotopes have been interpreted as spherical-shell model intruder states, created by π(4p-1h) proton excitations across the $Z = 82$ shell gap, resulting in a proton hole in the $s_{1/2}$ orbital [10–15]. Alternatively, in the deformed shell-model approach, such $1/2^+$ states are associated with the population of oblately deformed Nilsson orbitals.

In the even-A astatine isotopes, isomeric states have been observed with spins and parities of $I^\pi = 3^+,6^+,7^+$, and 10^- [16]. The structures of these states are expected to be similar to those of the even-A bismuth and thallium isotopes of the same spin. Thus, the odd proton is expected to occupy either a $\pi h_{9/2}$ or $\pi s_{1/2}$ state, coupled to the odd neutron occupying one of the low-lying $\nu p_{1/2}$, $\nu p_{3/2}$, $\nu f_{5/2}$, or $\nu i_{13/2}$ orbitals.

The main goal of the present work is the laser-spectroscopy study of the long chain of astatine isotopes, down to ^{195}At where an abrupt change in nuclear structure is expected to occur. The structure of the paper is as follows: In Sec. II, the experimental methods are detailed; Sec. III presents a description of the analysis of the hfs spectra, and the extraction of the nuclear parameters (further details may be found in the Appendix); the results for the respective nuclear electromagnetic moments and charge radii can be found in Sec. IV; the discussion of the results compared to other nuclei in the lead region is provided in Sec. V; concluding remarks are made in Sec. VI.

II. EXPERIMENTAL DETAILS

A. Beam production

The IS and hfs measurements of radioactive $^{195-211}$At were performed at the ISOLDE facility (CERN) [17], using the in-source resonance-ionization technique [18,19]. Astatine nuclei were produced in spallation reactions induced by the 1.4-GeV proton beam (with an average current of up to 2 μA) from the CERN PS Booster impinging on a thick UC_x target (50 g/cm^2 of ^{238}U). The spallation products effused out of the

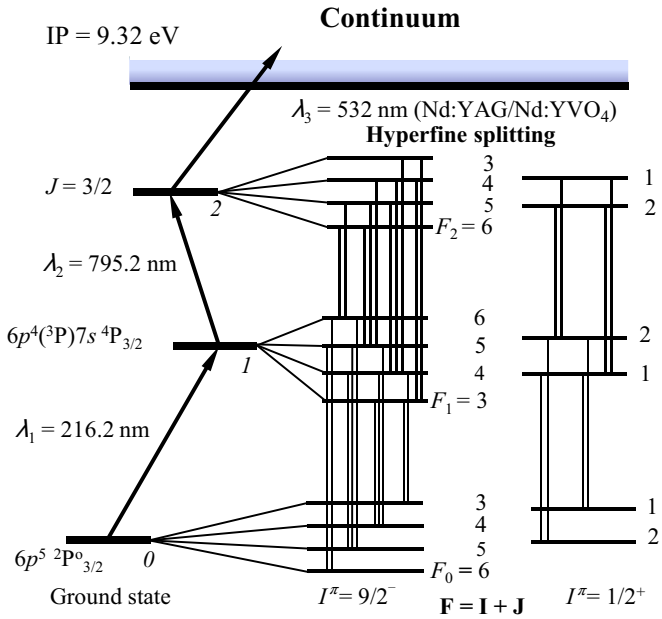

FIG. 1. The three-step laser-ionization scheme (levels labeled from 0 to 2) for astatine [1,2]. The electronic configurations for the levels involved and the laser wavelengths in air for each step are shown. The hfs for the $9/2^-$ and $1/2^+$ states of odd-mass astatine isotopes are shown schematically (not to scale). The scanning of the hfs was performed for both the 216.2- and 795.2-nm transitions.

high-temperature target ($T \approx 2050\,^\circ$C) as neutral atoms into the hot cavity of the Resonance Ionization Laser Ion Source (RILIS) [20,21]. The astatine atoms were ionized within the laser-atom interaction region of the hot cavity by applying the three-step astatine photoionization scheme shown in Fig. 1. The ionization efficiency of this scheme, with all three steps in broadband mode, is estimated to be higher than 4% [22]. The range of the yields of the investigated isotopes of astatine was from ≈20 ions/s (^{195}At using the WM), to ≈30 pA (^{205}At using the FC).

B. Photo-ion monitoring

After selective laser photoionization, the radioactive ions of interest were extracted and accelerated to 30 keV, mass separated by the ISOLDE high-resolution separator, and subsequently delivered to a counting station. For photo-ion monitoring, three methods were used: the ISOLDE Faraday cup (FC), for direct current measurements; the Windmill (WM) chamber, for α/γ decay measurements of relatively short-lived isotopes with $T_{1/2} < 1$ min; and the MR-TOF MS of the ISOLTRAP experimental setup, for further mass separation and subsequent ion counting [5]. In all three cases, the count rate of the photo-ion beam was monitored, while the frequency, ν_L, of the laser exciting the atomic transition of interest was scanned.

A detailed account of hfs scanning with the Windmill setup can be found in Refs. [6,7]. The following will describe how hfs measurements were performed using the MR-TOF MS device.

1. The MR-TOF MS

The MR-TOF MS was used for cases where the isotope of interest was either too long-lived, the α-decay branching ratio was unfavorable, or the levels of isobaric contamination from surface-ionized francium were too high for measurements to be performed using the Windmill system or a Faraday cup. The suppression of isobaric contamination was the very reason for implementing the MR-TOF MS at ISOLTRAP, with high-purity samples being an important condition in the context of precision mass spectrometry in Penning traps [23]. A schematic overview of the MR-TOF MS is shown in Fig. 2(a).

The mass-separated ion beam from ISOLDE was first delivered to the ISOLTRAP's radio-frequency quadrupole (RFQ) cooler and buncher [24], and then ejected as a bunch toward the MR-TOF MS, with a typical bunch width of 60 ns and energy spread of 60 eV. The cooled and bunched ions were then trapped inside the MR-TOF MS and separated into their isobaric constituents, following typically 1000 reflections between the electrostatic mirrors of the device. The ions were then extracted from the cavity and detected with an electron multiplier situated behind the MR-TOF MS, obtaining a well-separated time-of-flight (TOF) spectrum [see Fig. 2(b)].

The ion-counting application of the MR-TOF MS differs qualitatively from the TOF measurements used for mass determinations [25–27], as the former requires a very linear response of the recorded count rate with the incident photo-ion current. Such a large dynamic range (suppression of contaminating ions with respect to the ions of interest) of ≈10^4 was achieved by employing a MagneTOF™ secondary electron multiplier ion detector (DM291, ETP, Ermington, Australia) and a multichannel scaler (p7887, Fast ComTec, München, Germany) time digitizer, both having ≈1 ns time resolution. In order to bring the number of simultaneously recorded ions within the range of linear counting (<10 ions per isobaric species), the accumulation time of the ions in the RFQ (beam gate) was reduced to a few tens of microseconds. This is a significantly shorter time window than that required for ion separation in the MR-TOF MS (≈30 ms). This reduction was compensated by running the MR-TOF MS at a frequency of 10 to 20 Hz (i.e., >10 ion bunches separated and detected per second), an operation mode that was previously exploited for ion stacking in a Penning trap, for high-precision mass measurements [28]. This mode of operation provides a crucial advantage for recording of high-statistic hfs spectra, in a similar measurement time to that required by the Windmill detection system, ensuring the MR-TOF measurements were unaffected by target-ion-source instabilities (in particular, of the laser setup). Furthermore, under this operation mode it was unnecessary to rescale the beam gate during a single hfs measurement, thus avoiding systematic errors due to beam-gate nonlinearity.

Figure 2(b) illustrates the $A = 210$ TOF spectrum separated by the MR-TOF MS and measured on the electron multiplier, for the peak ionization efficiency of ^{210}At. Even at the maximum ^{210}At ionization rate, the contamination from ^{210}Fr is ≈6 times larger. Nevertheless, the francium peak is completely separated by the MR-TOF MS and a mass-resolving power of ≈1.7×10^5 was achieved. By placing an appropriate TOF gate, it was possible to count the photoionization efficiency of astatine, in a quasi-background-free manner.

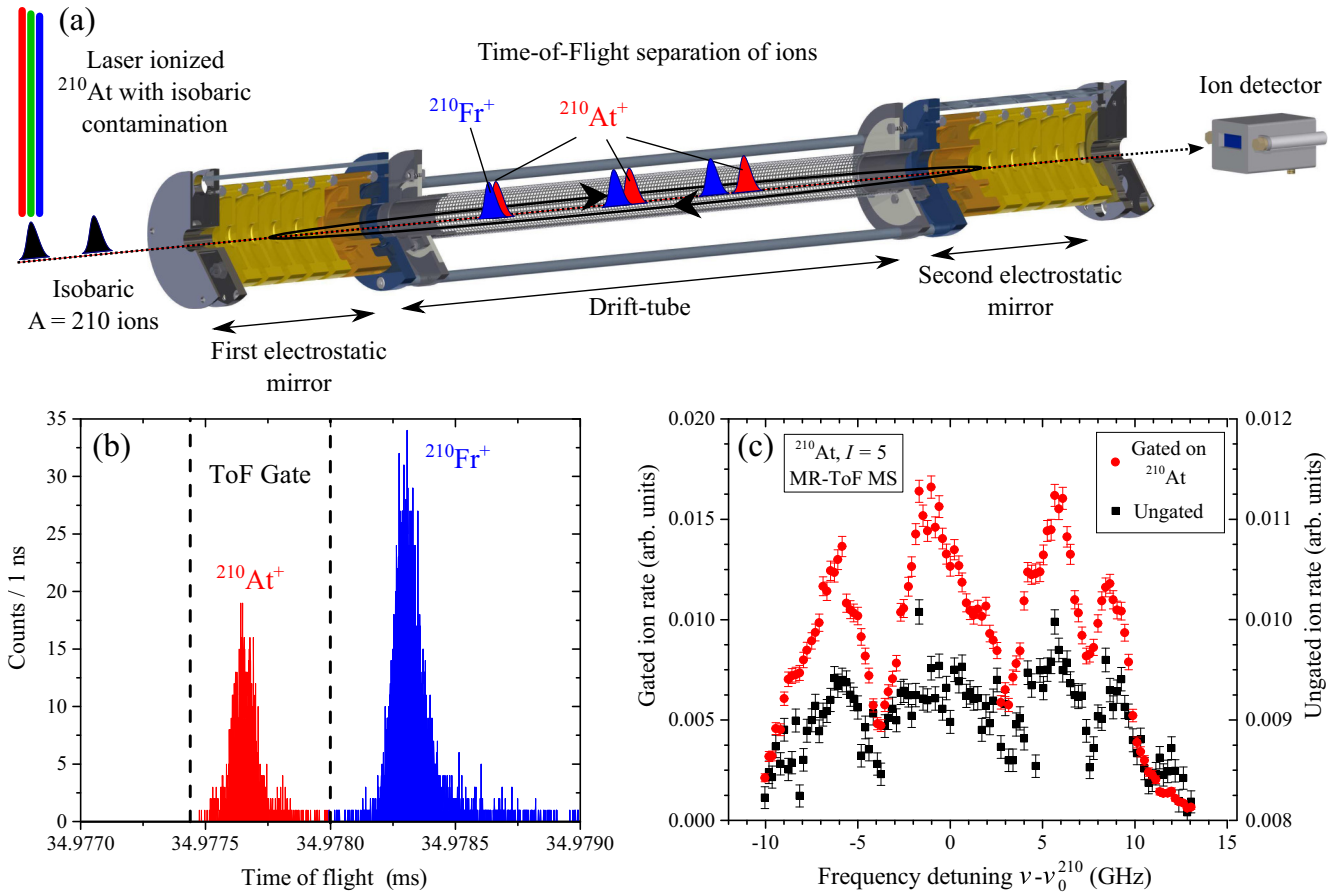

FIG. 2. (a) A schematic overview of the MR-TOF MS device in operation for a scan of ^{210}At, (b) an example of a typical time-of-flight (TOF) spectrum, and (c) the recorded hfs spectra, with (red circles) and without (black squares) a TOF gate placed on the ^{210}At ions, with intensities normalized for clarity. A mixed-species ion bunch (black bunches) from the RFQ enters the drift-tube of the MR-TOF MS through the central aperture of the first electrostatic mirror with an energy of ≈3.2 keV, before being decelerated by the in-trap lift electrode to ≈2 keV. The ions are then reflected multiple times between two electrostatic mirrors, separating the isobaric ^{210}At (red) and ^{210}Fr (blue) constituents temporally, in accordance with the difference in their respective masses. The separation process takes ≈35 ms, providing a mass-resolving power of $\approx 1.7 \times 10^5$ (a maximum resolving power of $\approx 3 \times 10^5$ has been achieved [29]). In order to extract the ion bunches, the voltage of a central in-trap lift electrode is switched when the ions are passing in the direction of the detector, thus ejecting them from the device. A high-resolution ion-counting system is then used to record a TOF spectrum, such as the one shown in panel (b). A TOF gate may then be placed in order to count the photo-ion production rate as a function of the scanned laser frequency, in order to produce hfs spectra such as that shown by the red circles in panel (c). The black squares in the plot in panel (c) represent how the hfs spectra would look without the placement of a TOF gate (i.e., without the mass-resolving capabilities of the MR-TOF MS).

The single-ion sensitivity of the electron multiplier alone was not sufficient to perform an adequate study of the highly contaminated astatine isotopes. To illustrate this, Fig. 2(c) shows the resulting hfs of ^{210}At before (black squares) and after (red circles) the TOF gate is applied. As can be seen from this plot, the fluctuations in count rate due to the francium background washes out the fine features of the hfs structure of ^{210}At. Thus, without the mass-resolving power of the MR-TOF MS, it would not have been possible to perform hfs and IS measurements on a number of the isotopes presented in this work.

C. In-source laser spectroscopy

The IS and hfs measurements were performed for two transitions ($\lambda_1 = 216.2$ and $\lambda_2 = 795.4$ nm; see Fig. 1). Examples of the hfs spectra from scanning the 216- and 795-nm transitions in ^{197}At^m ($I = 1/2$) are shown in the top and bottom panels of Fig. 3, respectively. Spectra obtained for selected astatine isotopes are shown in Fig. 4 (216 nm) and Fig. 5 (795 nm). The hfs of the second transition was better resolved than that of the first and is therefore more suitable for hfs-constants measurements. However, atomic calculations are usually much more reliable for the atomic ground states than for excited states, due to the increase in the number of valence electrons in excited states. The measurements for two different transitions enable us to check the validity of the atomic calculations (see Secs. IV B and IV C).

For IS and hfs measurements of the $\lambda_1 = 216$-nm transition, a frequency-tripled scanning dye laser in a narrowband mode (linewidth of ≈1 GHz before frequency tripling) was used, while a titanium:sapphire (Ti:Sa) laser operated in a broad-

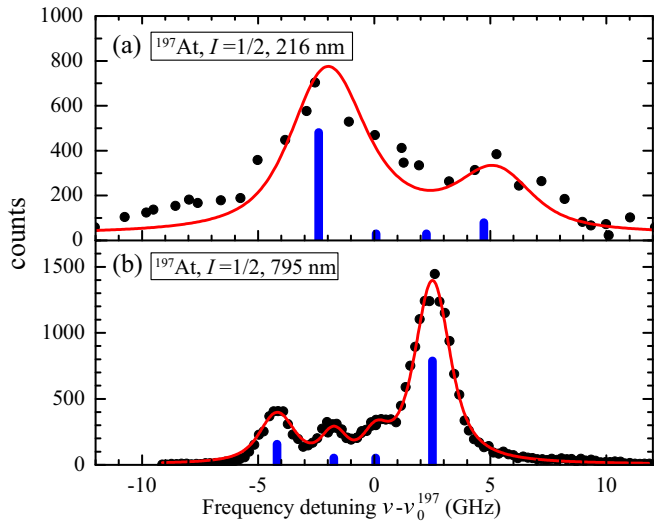

FIG. 3. Examples of experimental spectra, collected of the (a) $\lambda_1 = 216$-nm transition and (b) $\lambda_2 = 795$-nm transition, for the $1/2^+$ isomeric state in ^{197}At. The measurements were performed by counting the number of α particles with $E_\alpha = 6705$ keV using the Windmill setup, as a function of the laser frequency detuning. Frequency detuning is shown with respect to the hfs centroids. The solid red lines represent a fit to the data. The calculated positions and expected relative intensities of the individual hyperfine components are indicated by the vertical blue bars.

band mode (≈5 GHz) was used to excite the $\lambda_2 = 795$-nm transition. For hfs measurements of the 795-nm transition, the frequency of the Ti:Sa laser was scanned in narrowband mode (linewidth of ≈1 GHz) and a broadband (≈12 GHz) frequency-tripled dye laser was used for the first excitation step. In both cases, either a Nd:YAG or Nd:YVO_4 laser was employed for a final nonresonant ionization step ($\lambda_3 = 532$ nm), and the power of the narrowband laser is reduced to avoid line broadening caused by saturation.

During the experimental campaign, hfs spectra of ^{205}At were recorded on a regular basis with a Faraday cup, or the MR-TOF MS, in order to check the stability of the experimental conditions. More details on the laser and detection setups are given in Refs. [7,19,30], and references therein.

III. EXPERIMENTAL DATA ANALYSIS

A. Position and relative intensities of hfs components

The positions of the hyperfine components, $\nu^{F,F'}$, are determined by the formulas [4]

$$\nu^{F,F'} = \nu_0 + \delta\nu^{F'} - \delta\nu^{F}, \tag{1}$$

where ν_0 is the position of the center of gravity of the hfs, the prime symbol denotes the upper level of the transition, and

$$\delta\nu^{F} = A\frac{C}{2} + B\frac{\frac{3}{4}C(C+1) - I(I+1)J(J+1)}{2(2I-1)(2J-1)IJ}, \tag{2}$$

where I is the nuclear spin, J is the atomic spin, $C = F(F+1) - I(I+1) - J(J+1)$, and F is the total angular momentum of the atom ($\mathbf{F} = \mathbf{I} + \mathbf{J}$). The parameters A and

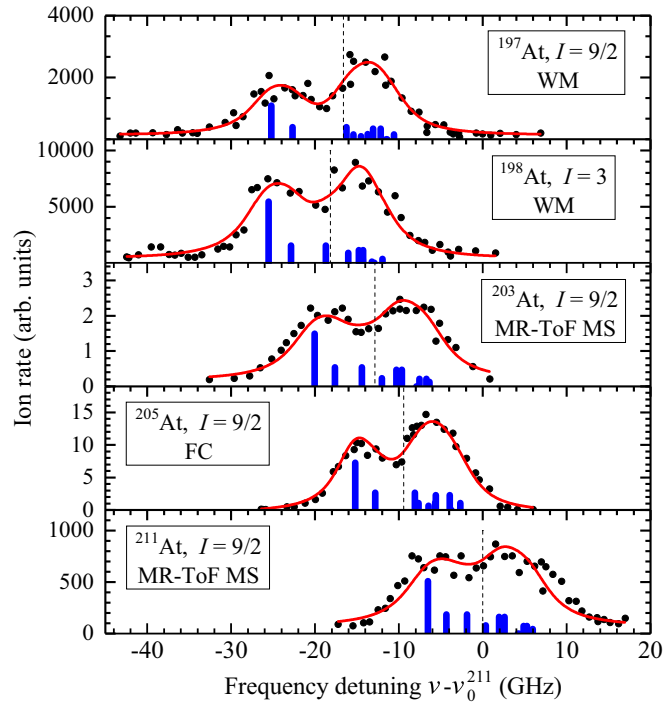

FIG. 4. Examples of experimental hfs spectra collected for the $\lambda_1 = 216$-nm transition, for (a) ^{197}At ($I = 9/2$), (b) ^{198}At ($I = 3$), (c) ^{203}At ($I = 9/2$), (d) ^{205}At ($I = 9/2$), and (e) ^{211}At ($I = 9/2$). Frequency detuning is shown with respect to the centroid of ^{211}At. The solid red lines represent a fit to the data. The vertical, black-dashed lines represent the center of gravity of the hfs. The vertical blue bars indicate the calculated positions, and expected relative intensities of the individual hyperfine components. The isotope the hfs belongs to, and the device used for the measurement are given in the insets.

B are the magnetic dipole and electric quadrupole hyperfine coupling constants, respectively:

$$A = \frac{\mu B_e(0)}{IJ}, \tag{3}$$

$$B = eQ_S\left\langle\frac{\partial^2 V_e}{\partial z^2}\right\rangle, \tag{4}$$

where $B_e(0)$ and $\langle\frac{\partial^2 V_e}{\partial z^2}\rangle$ are the magnetic field and the electric field gradient produced by the electrons at the site of the nucleus, respectively.

To take into account the saturation of transitions, pumping processes between hfs components, and population redistribution of hfs levels, the experimental hfs spectra were fitted using a similar method to that described in Ref. [7] for the polonium isotopes. In this work, additional considerations were made for the polarization of the laser light and possible detuning of the broadband laser radiation from the resonance. A detailed description of the fitting procedure is given in the Appendix.

B. Hyperfine splitting constants

Prior to this work, there existed no experimental data for hyperfine coupling constants of any atomic level of astatine. Therefore, in order to determine the proper A- and B-constant

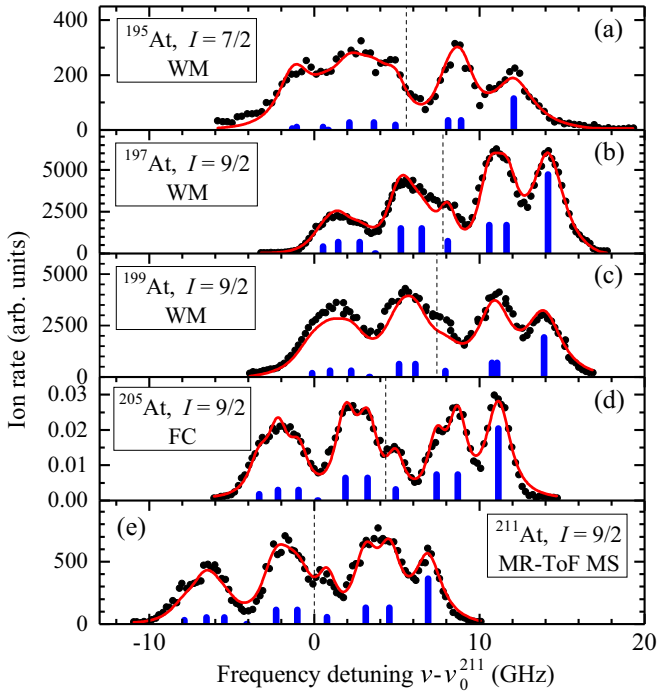

FIG. 5. Same as Fig. 4, but for scans of the $\lambda_2 = 795$-nm transition for (a) ^{195}At ($I = 7/2$), (b) ^{197}At ($I = 9/2$), (c) ^{199}At ($I = 9/2$), (d) ^{205}At ($I = 9/2$), and (e) ^{211}At ($I = 9/2$).

ratios, it was necessary to perform a preliminary analysis of the hfs for chosen isotopes.

1. The 795-nm transition

The limitation on the resolution of in-source laser spectroscopy due to Doppler broadening of the spectral lines prevents the separation of individual hyperfine components in the hfs spectra of high-spin nuclei (see Fig. 5). As the hfs of astatine isotopes have not been measured prior to this study, there are no high-resolution data available to fix the ratios of the hyperfine constants for the upper and lower electronic levels of the transition used in this study (as, for example, was done in the case of thallium nuclei [31]). Instead, the well-resolved hfs spectra for the ^{197}At^m ($I^\pi = 1/2^+$) and the hfs spectra for ^{205}At ($I^\pi = 9/2^-$) obtained with high statistics were used in order to fix these ratios for all other isotopes of astatine.

For ^{197}At^m ($I = 1/2$), the quadrupole hfs coupling constant B equals zero and all four hfs components were observed in the 795-nm line (see Fig. 3). From the relative intensities and frequency ordering of the hfs components, the signs of the magnetic hfs constants can be determined: $A_1 < 0$ and $A_2 > 0$ (here, and throughout the text, the indices correspond to the level numbering used in Fig. 1). Analysis of the spectra recorded when the 216-nm laser radiation was frequency detuned from the resonance position allowed for the unambiguous determination of the frequency ordering of all hfs components and the conclusion that $|A_1| < |A_2|$. Fitting the ^{197}At^m ($I = 1/2$) spectra with these constraints gave $A_2/A_1 = -1.73(2)$. This fixed A-constant ratio was used for the fitting of the other $I = 1/2$ nuclei (^{195}At^g, ^{199}At^m).

The collected statistics for the reference isotope ^{205}At, combined with the aforementioned restrictions on the A_1 and A_2 values, were sufficiently high to accurately determine the ratio of the magnetic hfs constants for $I = 9/2$ states: $A_2/A_1 = -1.69(2)$. The ratio of quadrupole hfs constants was also estimated: $|B_2/B_1| < 0.1$. In the fitting of the hfs spectra for states with $I > 1/2$, the A_2/A_1 ratio of hfs constants was fixed to those of ^{205}At ($I = 9/2$).

The possible change of the A-constant ratio for the $I \neq 9/2,\ 1/2$ is less than 1.2% (from comparison of A_2/A_1 for the $I = 9/2$ and $I = 1/2$ isotopes where this change is expected to be largest). The change of the fixed ratio A_2/A_1 leads to the corresponding change of the A_1 factor (which was varied during fitting). In order to account for this possible variation of the A_2/A_1 ratio, an additional uncertainty of 1.2% for $I \neq 9/2,\ 1/2$ nuclei was added to the experimental A factors.

2. The 216-nm transition

The hfs components of the 216-nm spectra were poorly resolved; therefore the corresponding values of A_1 and B_1 obtained by fitting 795-nm spectra were used. The ratio A_1/A_0 was determined from fitting hfs of ^{197}At^m with $I = 1/2$: $A_1/A_0 = -0.54(8)$. This ratio was fixed for the fitting of 216-nm transition spectra, for all astatine isotopes. Using this fixed A_1/A_0 ratio, the ratio of quadrupole hfs constants was determined: $B_0/B_1 = -5(2)$. The values obtained for the hfs coupling constants (A_1 and B_1) and IS for both of the scanned transitions are reported in Table I.

In the fitting procedure, the spins for the majority of the investigated isotopes were fixed in accordance with Ref. [16]. In the case of ^{202}At^g, the $I = 3$ spin assignment of Ref. [32] was used. For ^{199}At^m, the results from Ref. [13] were taken into account. The discussion and justification for the ^{206}At $I = 6$ spin assignment is given in Sec. V A 3.

IV. EXTRACTION OF NUCLEAR PARAMETERS

A. Magnetic moments

The nuclear magnetic moments can be calibrated using the known moments of another isotope of the element under study, via the ratio (see Ref. [33])

$$\mu = \mu_{\rm ref}\frac{I}{I_{\rm ref}}\frac{A}{A_{\rm ref}}(1 + {}^{\rm ref}\Delta^A), \tag{5}$$

where the index ref points to the reference isotope with the independently measured magnetic moment $\mu_{\rm ref}$ and ${}^{\rm ref}\Delta^A$ is the relative hyperfine structure anomaly (HFA) stemming from the finite charge and magnetization distribution inside the nucleus [34]. This parameter is dependent on both the nuclear and atomic states. In particular, the HFA reveals itself in the change in the ratio of the A constants for different atomic levels with the change of atomic mass and nuclear spin. Generally, the HFA is less than 1%. The observed difference of the order of 1% between A_2/A_1(^{197}At^m, $I = 1/2$) and A_2/A_1(^{205}At^g, $I = 9/2$) (see Sec. III B 1) may be regarded as the indication of the applicability of this estimation in the astatine case. For the states with the same spin and similar magnetic moment, the HFA is usually less than 0.1%. Correspondingly, an additional

TABLE I. Measured values of the hyperfine splitting constants and isotope shifts for the studied astatine isotopes. Statistical errors from the fitting of the hfs data are given in round brackets. For isotopes with $I \neq 9/2,\ 1/2$ an additional uncertainty of 1.2% due to indeterminacy of A-constants ratio is added. The values of $T_{1/2}$ are taken from Ref. [16].

Nucleus	I^π	$T_{1/2}$	$A(^4P_{3/2})$ (MHz)	$B(^4P_{3/2})$ (MHz)	$\delta\nu_{216}^{205}$ (MHz)	$\delta\nu_{795}^{205}$ (MHz)	Detection method
^{195}At^g	$(1/2^+)$	290(20) ms	−1287(20)			2050(75)	WM
^{195}At^m	$(7/2^-)$	143(3) ms	−424(11)	−1221(150)		1251(75)	WM
^{196}At	(3^+)	387(14) ms	−498(15)	−382(80)		3086(120)	WM
^{197}At^g	$(9/2^-)$	381(6) ms	−342(4)	−690(50)	−7190(750)	3466(75)	WM
^{197}At^m	$(1/2^+)$	2.0(2) s	−1235(10)		−2975(750)	1598(75)	WM
^{198}At^g	(3^+)	4.1(3) s	−538(12)	−353(90)	−8731(750)	3944(75)	WM
^{198}At^m	(10^-)	1.03(15) s	−102(3)	261(150)		3675(75)	WM
^{199}At^g	$(9/2^-)$	6.92(13) s	−351(4)	−573(50)		3099(75)	WM
^{199}At^m	$(1/2^+)$	310(80) ms	−1275(30)			912(120)	WM
^{200}At^g	(3^+)	43(1) s	−570(13)	−302(50)		3408(75)	WM
^{200}At^{m1}	(7^+)	47(1) s	−271(7)	−578(70)		3222(75)	WM
^{200}At^{m2}	(10^-)	3.5(1) s	−108(3)	323(150)		3003(100)	WM
^{201}At	$(9/2^-)$	83(2) s	−357(4)	−574(90)		2299(75)	MR-TOF MS
^{202}At^g	(3^+)	184(1) s	−554(16)	−325(80)		2649(120)	WM
^{202}At^m	(7^+)	182(2) s	−259(9)	−392(80)		2330(120)	WM
^{203}At	$9/2^-$	7.4(2) min	−357(4)	−437(50)	−3437(900)	1332(75)	MR-TOF MS
^{204}At	7^+	9.22(13) min	−0.276(7)	−372(50)		1257(75)	MR-TOF MS
^{205}At	$9/2^-$	26.9(8) min	−365(3)	−367(50)	0	0	MR-TOF MS, FC
^{206}At	(6^+)[a]	30.6(8) min	−292(9)	−254(60)		−242(75)	MR-TOF MS
^{207}At	$9/2^-$	1.80(4) h	−368(4)	−273(50)	2201(900)	−1334(75)	MR-TOF MS
^{208}At	6^+	1.63(3) h	−298(10)	−238(150)		−1801(75)	MR-TOF MS
^{209}At	$9/2^-$	5.41(5) h	−368(4)	−241(50)	6232(750)	−2788(75)	MR-TOF MS
^{210}At	$(5)^+$	8.1(4) h	−379(10)	−253(70)		−3427(75)	MR-TOF MS
^{211}At	$9/2^-$	7.214(7) h	−367(4)	−201(70)	9423(900)	−4318(100)	MR-TOF MS

[a]For $I = 5$, $\delta\nu_{795}^{205} = -117(75)$ MHz, $A = -347(10)$ MHz, and $B = -176(60)$ MHz. Spin assignment for ^{206}At is discussed in Sec. V A 3.

1% error was added to the magnetic moments for astatine isotopes with $I \neq 9/2$, and 0.1% error for isotopes with $I = 9/2$, since the reference ^{211}At has $I = 9/2$.

There are no data available for the magnetic moments of ground states in isotopes of astatine, and therefore the experimental g factor of the high-spin nuclear isomeric state with $I^\pi = 21/2^-$ in ^{211}At was used as a reference. This isomeric state belongs to the lowest seniority $\nu = 3$ states in ^{211}At, and is formed by three $h_{9/2}$ protons coupled to $[h_{9/2}^3]_{21/2^-}$.

A number of experimental and theoretical investigations have proven the admixtures of states belonging to other configurations and to collective excitations to this high-spin state in all $N = 126$ isotones to be small [35–38]. For these pure states, the additivity rule (see Ref. [39]) is applicable: $g(h_{9/2}^n) = g(h_{9/2})$. The purity of the corresponding states is supported by the similarity of the experimental g factors of the $h_{9/2}^3$ high-spin states ($21/2^-$ and $17/2^-$) with the g factor of the $h_{9/2}$ ground state in ^{213}Fr$_{126}$: $g(9/2^-, {}^{213}\mathrm{Fr}^g) = 0.885(11)$;[1] $g(21/2^-, {}^{213}\mathrm{Fr}^m) = 0.888(3)$ [42]; and $g(17/2^-, {}^{213}\mathrm{Fr}^m) = 0.88(16)$ [36].

Similarly, the g factor of the $\pi h_{9/2}$ ground state of ^{211}At ($N = 126$) should be equal to the $g(h_{9/2^-})$ values extracted from the high-spin data, using the simple shell-model rules. The g factors of the high-spin isomers in ^{211}At were measured in Ref. [43], $g(21/2^-, {}^{211}\mathrm{At}^m) = 0.917(18)$ and in Ref. [44], $g(21/2^-, {}^{211}\mathrm{At}^m) = 0.921(9)$.[2] The weighted mean of the results from Refs. [43,44] is $g(h_{9/2}) = g(21/2^-, {}^{211}\mathrm{At}) = 0.920(9)$. The corresponding magnetic moment value, $\mu({}^{211}\mathrm{At}^g) = 4.139(37)\ \mu_N$, was used as a reference in Eq. (5). The same approach was applied in Ref. [45] for actinium isotopes. Magnetic moments calculated using Eq. (5) are presented in Table II. Systematic errors stemming from the HFA and the uncertainty in the μ_{ref} value are given in curly brackets.

To check the validity of the choice of μ_{ref}, the g factor for isomers with $I^\pi = 29/2^+$ in astatine, francium, and actinium were calculated using the additivity relation with $g(h_{9/2}) = g(21/2^-)$. These isomers are supposed to have a pure $[(h_{9/2}^2)_8 \otimes i_{13/2}]$ configuration [35]. The g factor for the $29/2^+$ isomers was calculated using $g(\pi i_{13/2}) = 1.246(20)$ from Ref. [36] (see also Ref. [46], and references therein). The results of the additivity-relation calculations agree with the experimental data [36,37,43,44] for $g(29/2^+)$ in ^{211}At, ^{213}Fr, and ^{215}Ac, within the limits of experimental uncertainties.

[1]Recalculated using $A(P_{1/2})$ hfs constants from Ref. [40] and using $\mu(^{210}\mathrm{Fr})$ from Ref. [41] as a reference.

[2]Recalculated with the diamagnetic shielding and Knight-shift corrections from Ref. [43]; an additional 20% error for the diamagnetic shielding and Knight-shift corrections is taken into account.

TABLE II. Extracted values of the change in mean-square charge radii, the mean-square deformation extracted from the IS data (see Sec. IV C), and the magnetic and quadrupole moments for astatine isotopes. Errors due to the statistical uncertainties in the extracted hyperfine parameters in Table I are given in round brackets. Systematic uncertainties are given in curly brackets, in $\delta\langle r^2\rangle$, stemming from the theoretical indeterminacy of the F and M factors for $\delta\langle r^2\rangle_{A,205}$; in μ, due to the uncertainty in $\mu_{\rm ref}$ and the HFA indeterimnacy; and in Q_S, resulting from the uncertainty in the theoretical B_0/Q_S, and the experimental B_1/B_0 ratios.

Nucleus	N	I^π	$\delta\langle r^2\rangle_{A,205}$ (fm^2)	β_{DM}	μ (μ_N)	Q_S (b)
^{195}At^g	110	$(1/2^+)$	−0.171(7){9}	0.21(2)	1.611(25){39}	
^{195}At^m	110	$(7/2^-)$	−0.101(7){5}	0.22(2)	3.714(97){90}	−2.04(25){100}
^{196}At	111	(3^+)	−0.262(10){13}	0.17(2)	3.739(110){90}	−0.64(13){35}
^{197}At^g	112	$(9/2^-)$	−0.296(7){15}	0.15(3)	3.849(45){54}	−1.15(8){60}
^{197}At^m	112	$(1/2^+)$	−0.133(7){7}	0.19(2)	1.546(13){37}	
^{198}At^g	113	(3^+)	−0.338(7){17}	0.11(4)	4.037(94){97}	−0.59(15){30}
^{198}At^m	113	(10^+)	−0.315(7){16}	0.12(3)	2.554(81){62}	0.44(25){25}
^{199}At^g	114	$(9/2^-)$	−0.265(7){13}	0.12(3)	3.955(45){56}	−0.95(8){50}
^{199}At^m	114	$(1/2^+)$	−0.075(10){4}	0.17(2)	1.595(38){39}	
^{200}At^g	115	(3^+)	−0.293(7){15}	0.08(4)	4.279(96){110}	−0.50(8){50}
^{200}At^{m1}	115	(7^+)	−0.277(7){14}	0.09(5)	4.74(13){12}	−0.96(12){50}
^{200}At^{m2}	115	(10^-)	−0.258(9){13}	0.10(4)	2.694(82){65}	0.54(25){30}
^{201}At	116	$(9/2^-)$	−0.197(7){10}	0.10(4)	4.025(45){57}	−0.96(15){50}
^{202}At^g	117	(3^+)	−0.229(10){11}	0.04(9)	4.16(12){10}	−0.54(13){30}
^{202}At^m	117	(7^+)	−0.201(10){10}	0.06(6)	4.54(16){11}	−0.65(13){30}
^{203}At	118	$9/2^-$	−0.115(7){6}	0.08(5)	4.021(45){57}	−0.73(8){35}
^{204}At	119	7^+	−0.109(7){5}	0.05(8)	4.84(13){12}	−0.62(8){30}
^{205}At	120	$9/2^-$	0	0.08(4)	4.111(34){58}	−0.61(8){30}
^{206}At	121	(6^+)[a]	0.020(7){1}	0.06(6)	4.39(13){11}	−0.42(10){20}
^{207}At	122	$9/2^-$	0.115(7){6}	0.08(4)	4.150(45){59}	−0.45(8){25}
^{208}At	123	6^+	0.155(7){8}	0.07(4)	4.48(14){11}	−0.40(25){20}
^{209}At	124	$9/2^-$	0.240(7){12}	0.09(3)	4.141(45){59}	−0.40(8){20}
^{210}At	125	$(5)^+$	0.295(7){15}	0.09(3)	4.74(12){11}	−0.42(12){20}
^{211}At	126	$9/2^-$	0.372(9){19}	0.09(2)	4.139(37)[b]	−0.33(12){20}

[a]For $I = 5$, $\delta\langle r^2\rangle_{A,205} = 0.009(7)\{1\}$ fm^2, $\mu = 4.34(12)\{11\}\,\mu_N$, $Q_S = -0.29(10)\{15\}$. Spin assignment for ^{206}At is discussed in Sec. V A 3.
[b]Reference value.

These results support the assumption that $g(21/2^-, {}^{211}\mathrm{At}^m) = g(9/2^-, {}^{211}\mathrm{At}^g)$.

Magnetic moments may be also evaluated using calculated values of $B_e(0)$ [see Eq. (3)], but in this case the systematic uncertainties would be much larger (see Sec. IV B 1 for more details).

B. Quadrupole moments

For astatine, there are no independently measured values of Q_S. Thus, the calibration of Q_S cannot be made with the same method as was used for the magnetic moments. To obtain Q_S from the measured hfs constant B, through the Eq. (4), the electric field gradient resulting from the electronic density at the nucleus has to be known. In the present work, this field gradient for the astatine atomic ground state was calculated by applying the multiconfiguration Dirac-Hartree-Fock (MCDHF) method [47]. In order to check the theoretical approach, the factor A/g was also calculated and compared with experimental results.

1. Hyperfine calculations with MCDHF theory

In the framework of the MCDHF approach, numerical-grid wave functions have been generated by means of the atomic structure code GRASP [48], as self-consistent solutions of the Dirac-Hartree-Fock equations [49]. The electrostatic electron-nucleus interaction was generated from a nuclear charge density distribution, which was approximated by the two-component Fermi function, normalized to Z [50]. All other nuclear electromagnetic moments were neglected. Breit and QED corrections [51] were neglected, since they are expected to be negligible at the current level of accuracy. The full description of numerical methods, virtual orbital sets, electron substitutions, and other details of the computations can be found in Refs. [52–55].

The results of the calculations are $A_0/g = 850(150)$ MHz and $B_0/Q_S = -3000(300)$ MHz/b, respectively. The accuracies of the final values have been estimated with the methods described in Ref. [54].

The theoretical (A_1/g) factor can be calculated using the simple relation:

$$\left(\frac{A_1}{g}\right)_{\rm theor} = \left(\frac{A_1}{A_0}\right)_{\rm exp}\left(\frac{A_0}{g}\right)_{\rm theor}, \tag{6}$$

where $(A_1/A_0)_{\rm exp} = -0.54(8)$ (see Sec. III B 2).

The calculated value $(A_1/g)_{\rm theor} = -460(150)$ MHz agrees fairly well in the limits of uncertainties with the experiment: $(A_1/g)_{\rm exp} = A_1({}^{211}\mathrm{At})\,I({}^{211}\mathrm{At})/\mu({}^{211}\mathrm{At}) = -399(13)$ MHz. This supports the B/Q_S-factor calculation. It is worth noting that in Ref. [56], B/Q_S factors for astatine homologues

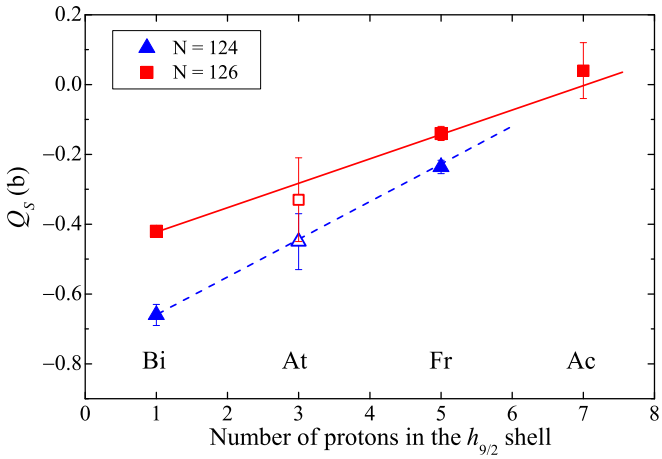

FIG. 6. Dependence of Q_S on the number of protons (n_π) in the $h_{9/2}$ shell, for astatine ($n_\pi = 3$, present work; hollow symbols); actinium ($n_\pi = 7$), [59]; francium ($n_\pi = 5$) [61]; and bismuth ($n_\pi = 1$) [62]. The blue triangles represent the $N = 124$, and the red squares represent the $N = 126$ isotopes.

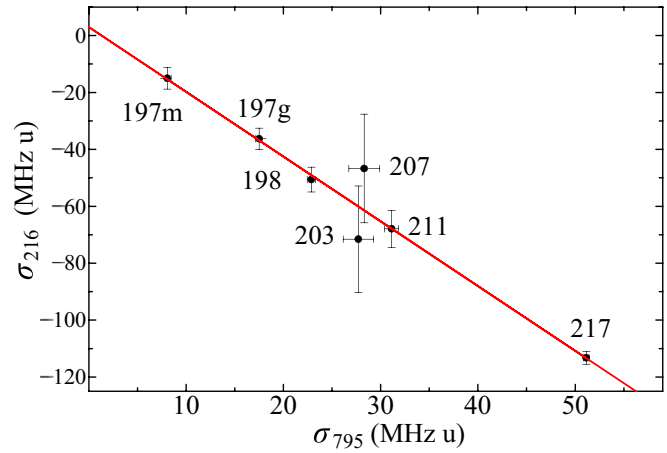

FIG. 7. King plot for the 216-nm vs 795-nm transitions. The red line is a linear fit of the data.

with different principal quantum number n (chlorine, $n = 3$; bromine, $n = 4$; iodine, $n = 5$) were calculated using the coupled cluster method. These results may be extrapolated to astatine ($n = 6$) assuming that the Z and n dependence of the B/Q_S factor may be described by the formulas from Ref. [57]. The result of the extrapolation, $B_0/Q_S = -3170$ MHz/b, agrees with the theoretical value quoted above.

2. *Values of* $\mathbf{Q}_S$ *extracted from the hyperfine data*

The Q_S values derived from the measured hfs quadrupole constants given in Table I are presented in Table II. Semimagic nuclei with $N = 126$ can be described by the seniority scheme [58]. In this framework, Q_S should have a linear correlation with the number of protons occupying the $h_{9/2}$ orbital. This linearity was confirmed in Ref. [59] for $Z = 83, 87, 89$. Our new data for $Q_S(^{211}\mathrm{At}_{126})$ fit to this straight line (see Fig. 6). The observed values of $Q_S(N = 126)$ nuclei are reproduced well by large-scale shell-model calculations [59]. In particular for $^{211}\mathrm{At}_{126}$, the theoretically calculated value of $Q_{S,\mathrm{theor}} = -0.266$ b [59,60] is in good agreement with the measured value of $Q_{S,\mathrm{exp}} = -0.33(12)$ b. The value of $Q_S(^{209}\mathrm{At}_{124})$ also follows the seniority-scheme systematics for $Q_S(N = 124)$ (see Fig. 6). These observations support the result of the B/Q_S-factor calculation and the magnitude of the ascribed errors. The agreement of $Q_S(^{211,209}\mathrm{At})$ with the seniority-scheme systematics within the experimental statistical errors suggests the estimated systematic uncertainty is too large. Therefore, in the discussion of quadrupole moments, only the statistical errors will be taken into account.

C. Changes in the mean-square charge radii

The IS between two nuclei is defined as

$$\delta\nu^{AA'} = \nu^A - \nu^{A'}, \tag{7}$$

where ν is the position of the center of gravity of the hfs belonging to isotopes A and A'. The change in the mean-square charge radii between two nuclei, $\delta\langle r^2\rangle_{AA'}$, is extracted from the measured $\delta\nu^{AA'}$ by the relations [63]

$$\delta\nu_\lambda^{A,A'} = F_\lambda \delta\langle r^2\rangle_{AA'} + M_\lambda \frac{A - A'}{AA'}, \tag{8}$$

where A and A' are the atomic mass numbers of the two isotopes, F_λ is the electronic factor, and M_λ is the mass factor, which is the sum of normal mass shift (NMS) constant $M_\lambda^{NMS} = \frac{\nu}{m_p/m_e}$ (ν is the transition frequency) and specific mass shift (SMS) constant M_λ^{SMS}.

The measurement of the IS for two different transitions allows one to draw a King plot [63]. Using such a plot allows for the consistency of the experimental data to be checked, by the comparison of the modified isotope shifts (see Fig. 7):

$$\sigma_\lambda^{A,A'} \equiv \delta\nu^{A,A'} \frac{AA'}{A - A'}. \tag{9}$$

Following Eq. (8), the modified isotope shifts for different pairs of isotopes should follow a straight line:

$$\sigma_{216}^{A,A'} = \kappa\sigma_{795}^{A,A'} + s. \tag{10}$$

The slope of this line is equal to the ratio of the electronic factors, $\kappa_{795}^{216} = F_{216}/F_{795}$, and the intersection of the regression line with the y axis is equal to the linear combination of the mass shift constants for the transitions involved:

$$s = M_{216} - \frac{F_{216}}{F_{795}} M_{795}. \tag{11}$$

The linear fit in Fig. 7 testifies to the consistency of the experimental data. Experimental values, $\kappa_{795}^{216} = -2.275(41)$ and $s_{795}^{216} = 2990(1600)$ GHz u, may be compared with the results of the corresponding theoretical calculations (see Table III). It should be noted that the ratio of the F factors for the similar transitions in polonium, $\kappa_{843}^{256} = -2.241(68)$ [64], proved to be very close to the astatine ratio.

To determine the M^{SMS} and F_λ parameters for the $\lambda_1 = 216$-nm and $\lambda_2 = 795$-nm transitions, large-scale MCDHF calculations were performed with the same tools and methods as those described in Sec. IV B 1. The operators for the hyperfine interaction and isotope shift in atoms are

TABLE III. Results of the large-scale MCDHF calculations (normal font) of the atomic factors of astatine. The values of κ_{795}^{216} and s_{795}^{216} extracted from the experimental data are included for comparison (bold font). Uncertainties for the computational models were estimated based on the stabilization of the results when going from one approximation to another.

Parameter	$\lambda = 216$ nm	$\lambda = 795$ nm
M^{SMS} GHZ u	690(350)	−580(100)
F MHz/fm^2	25 200(2600)	−11470(570)
κ_{795}^{216}	−2.19(15)	
	−2.275(41)	
s_{795}^{216}	630(640)	
	2990(1600)	

different, and thus their sensitivities to different types of electron correlations also differ [65]. For heavy atoms, it is impossible to include all important electron-correlation effects. Therefore, in hfs and IS calculations, one should use different wave functions constructed in the framework of different approaches to electron correlations. It is for this reason that two types of large-scale atomic calculations were applied, one for calculating the IS and the other for the hfs. Similar to the above, systematically enlarged wave function expansions were applied. These included core polarization and core-valence correlations to compute these isotope parameters and to obtain insight into their convergence [66]. Different computational models were used and different classes of correlations were incorporated into the isotope-shift parameters [67]. Although the individual results for the specific mass- and field-shift parameters seem to stabilize with the size of the expansion, it was not possible to demonstrate a real convergence. The results of these computations are shown in Table III.

The agreement with experiment for the F-factor ratio κ is excellent. However, as described in Ref. [68], even uncorrelated Dirac-Fock calculations often reproduce ratios of F factors quite well. The absolute precision of the calculated F factors is still a matter of discussion. The agreement for the combined mass-shift factor, s, may be regarded as reasonable (in the limit of 1.5 $\sigma_{\rm exp}$). A similar agreement was observed in the neighboring polonium chain ($Z = 84$), where similar calculations were performed and compared to experimental results [64].

The validity of the calculated F factor may be checked by comparison with the results for the adjacent isotopic chains. One can expect that the change in the mean-square charge radius between isotopes with neutron numbers N_1 and N_2, $\delta\langle r^2\rangle_{N_1,N_2}$, has a simple Z dependence, at least for $N_1, N_2 = 126, 124$ due to the proximity of the closed neutron shell. This assumption was confirmed in Ref. [31] by the analysis of the available IS data for some elements in the lead region. Remarkably, the Z dependence of $\delta\langle r^2\rangle_{126,124}$ for $Z = 80$–88 follows a simple parabolic law [31]. Recently measured IS for several actinium isotopes ($Z = 89$) [59] enabled the determination of $\delta\langle r^2\rangle_{126,124}$ for $Z = 89$ by the application of large-scale atomic calculations similar to those in the present paper. This new point lies on the continuation

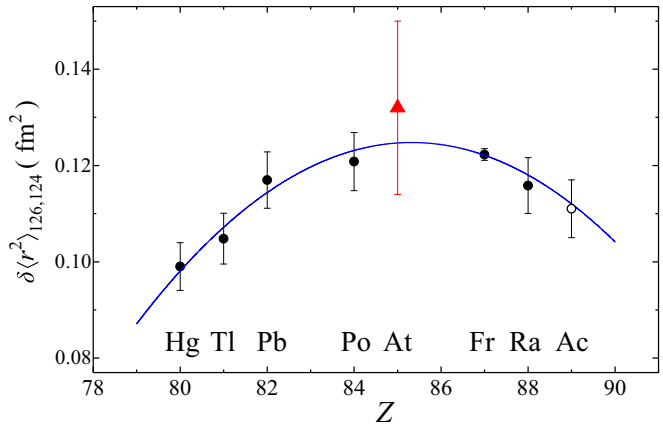

FIG. 8. Z dependence of $\delta\langle r^2\rangle_{126,124}$. Experimental data for $Z = 80$–$82, 84, 87, 88$ (black filled circles, see Ref. [31] and references therein) and Ac ($Z = 89$, hollow black circle) [59]. The data point for astatine ($Z = 85$, red triangle) was calculated using $F_{795} = -11470(570)$ MHz/fm^2 and $M_{795}^{SMS} = -580(100)$ GHz u, taking into account both statistical and systematic errors. The blue curve is the parabolic fit described in Ref. [31].

of the parabolic fit for $Z = 80$–88 from Ref. [31] (see Fig. 8), which substantiates the presumed parabolic Z dependence of $\delta\langle r^2\rangle_{126,124}$.

The value of $\delta\langle r^2\rangle_{126,124}$ ($Z = 85$) calculated using Eq. (8), with F and M factors for the 795-nm transition in astatine, follow the same parabolic curve (see Fig. 8). This may be regarded as additional supporting evidence of the validity of the atomic calculations for the astatine F factor, and the assigned uncertainties.

The values of $\delta\langle r^2\rangle$, evaluated from the measured IS and the calculated F and M factors, are presented in Table II.

It is generally acknowledged that the main isotopic trend of the $\delta\langle r^2\rangle$ is described by the droplet model (DM) (see Ref. [69] and references therein). Deviations from the DM trend can be attributed to the development of the mean-square quadrupole deformation ($\langle\beta^2\rangle$):

$$\langle r^2\rangle = \langle r^2\rangle_{DM}\left(1 + \frac{5}{4\pi}\langle\beta^2\rangle\right), \tag{12}$$

where $\langle r^2\rangle_{DM}$ is the mean-square charge radius calculated by DM with zero deformation. The values of $|\beta_{DM}| \equiv \langle\beta^2\rangle^{1/2}$ were calculated using Eq. (12) from experimental $\delta\langle r^2\rangle$ values with DM parameters taken from Ref. [69] and setting $|\beta|(^{209}\text{At}) = |\beta|(^{208}\text{Po}) = 0.086$ (see Ref. [70]). The values of β_{DM} are presented in Table II.

V. DISCUSSION

Similar $1/2^+$ intruder states to those found in the astatine isotopes are well known in neighboring isotones, such as bismuth ($Z = 83$) nuclei, in which they are created by π(2p-1h) excitations [10]. In the bismuth isotopes, the excitation energies of the $1/2^+$ intruder states decrease approaching the $N = 104$ (^{187}Bi) neutron midshell [71]. Moreover, this intruder state becomes the ground state in ^{185}Bi [72–74]. It was suggested that this downward trend in the energy of the

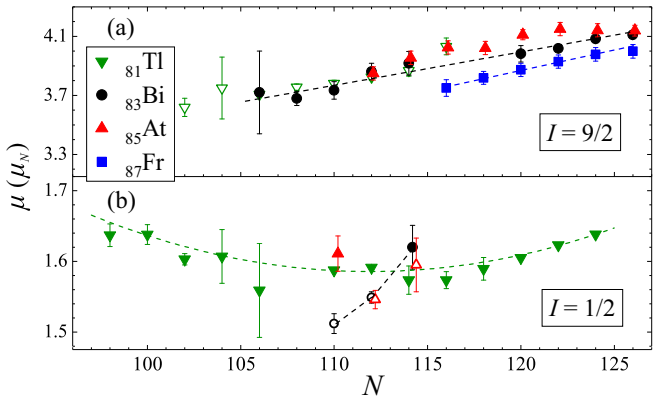

FIG. 9. Magnetic dipole moments for (a) the $9/2^-$ and (b) $1/2^+$ states of the odd-A astatine (red triangles; present work), thallium (green downward triangles; Ref. [78] and references therein), bismuth (black circles) [31,62,79], and francium (blue squares) [61,80,81] isotopes. The filled and hollow symbols indicate ground and isomeric states, respectively. The dashed lines are to guide the eye only.

intruder isomers in bismuth could arise from the crossing of two different $1/2^+$ states [74]; a prolate-deformed $1/2^+$ state, associated with a $1/2^+[660]$ Nilsson orbital, would cross the weakly oblate-deformed intruder state, producing the observed reduction in energy of the $1/2^+$ state.

The possible analogy with the $1/2^+$ intruders in the bismuth chain could be an important one for the astatine nuclei. A similar mechanism could be responsible for the downward trend of astatine intruder-state energies. The measurement of the magnetic moment for the $1/2^+$ states would help in the unravelling of this possible admixture of oblate-prolate configurations.

A comparison of astatine and polonium ($Z = 84$) isotopes can also be instructive, since the former can be considered as produced by coupling an extra proton to the underlying polonium core. Earlier measurements of the polonium charge radii showed an onset of deformation from ^{199}Po ($N = 115$) onward [7,64,70]; thus, a similar deformation effect can be expected in the astatine chain. Indeed, the systematics of low-lying states in polonium isotopes prove to be remarkably similar to those of the corresponding astatine nuclei [75,76]. In particular, the drop in the excitation energy of the 2^+ states when going from ^{200}Po to ^{196}Po was found to be analogous to the behavior of $11/2^-$ states in $^{201-197}$At. This decrease in energy has been interpreted as evidence for an increase in collectivity and an onset of deformation near ^{196}Po and ^{197}At, respectively.

A. Magnetic moments

1. Odd-A states with $I^\pi = 1/2^+$ and $9/2^-$

In Fig. 9, the magnetic moments of the odd-A astatine ground and isomeric states with $I^\pi = 9/2^-$ and $I^\pi = 1/2^+$ are compared with the magnetic moments of states with equal spin in francium, bismuth and thallium. The magnetic moments of the $9/2^-$ states follow a linear, weakly decreasing A dependence [see Fig. 9(a)], with a trend toward the Schmidt value ($\mu_S = 2.6\ \mu_N$) below $N = 126$. This linear dependence may be attributed to the decrease of the first-order core-polarization correction – a result of the gradual decrease in the occupancy of the $\nu i_{13/2}$ shell. This explanation is similar to that of Ref. [77], where this mechanism was applied for the explanation of the similar A dependence of the $(\nu i_{13/2})^{-n}$ Pb-isomer g factor. It is worth noting that the slope of the corresponding N dependencies is the same for the thallium, bismuth, and astatine isotopes [see Fig. 9(a)]. This constancy supports the proposed interpretation. It is important to note the independence of the magnetic moments on the nature and deformation of the state, as $I = 9/2^-$ is a deformed intruder in the thallium isotopes, while it is predominantly a spherical (at least around $N = 126$), ground state in bismuth, astatine, and francium (see also Ref. [39]).

The magnetic moments of the $1/2^+$-intruder states in astatine are in good agreement with $\mu(1/2^+)$ of the thallium and bismuth isotopes [see Fig. 9(b)], with all values lying in a narrow range of $\mu = 1.5$–$1.65\ \mu_N$. Similar to the $I = 9/2$ states, we note the independence of the $\mu(1/2^+)$ values on the nature and deformation of the states; the $I = 1/2^+$ state is the normal, spherical ground state in thallium, while it is an excited deformed intruder state in bismuth and astatine.

It was proposed earlier that the violation of the parabolic N dependence of the $1/2^+$ excitation energy, in, e.g., ^{185,187}Bi, may be connected to the admixture of the prolate $1/2^+$ state, associated with a $1/2^+[660]$ Nilsson orbital, with the weakly oblate-deformed $1/2^+[400]$ state [74]. A similar mechanism could be considered for the lightest astatine isotopes. However, as $\mu(1/2^+[660]) > 3\ \mu_N$ at $\beta > 0.15$ (Nilsson model calculations; see details in Ref. [7]), the assumed admixture would lead to a noticeable increase of the magnetic moment in the astatine chain, which is not observed in our data.

2. ^{195}At^m, ($I^\pi = 7/2^-$)

The measured magnetic moment $\mu_{\rm exp}(^{195}\text{At}^m) = 3.71(10)\ \mu_N$, is reasonably close to $\mu_{\rm theor}(7/2^-[514]) = 3.2\ \mu_N$. The latter value was calculated using the standard Nilsson model (see details in Ref. [7]), and represents the magnetic moment of a one-particle state, with the odd proton occupying the $7/2^-[514]$ Nilsson orbital at a quadrupole deformation $\beta_2 = -0.2$. A rotational gyromagnetic ratio, $g_R = 0.4$, and the standard renormalization, $g_s = 0.7 g_s^{\rm free}$, were used in these derivations.

The difference between the experimental and theoretical values could be due to Coriolis mixing, which should be taken into account for high-spin states with a moderate deformation. Within the framework of the particle-plus-rotor model (see details in Ref. [7]), $\mu_{\rm theor}(7/2_1^-) = 3.8\ \mu_N$ for the lowest $7/2^-$ state with a predominantly $7/2^-[514]$ Nilsson configuration. This theoretical value is in good agreement with $\mu_{\rm exp}(^{195}\text{At}^m) = 3.71(10)\ \mu_N$, which supports the proposed interpretation of the ^{195}At^m as an oblately deformed state, with the odd proton primarily occupying the $7/2^-[514]$ Nilsson orbital [8].

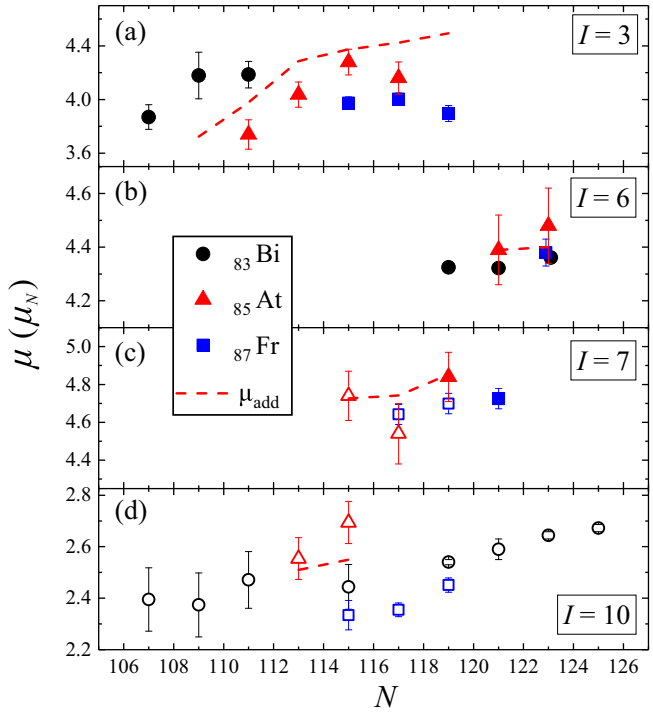

FIG. 10. The magnetic dipole moments for the (a) 3^+ ($\pi h_{9/2} \otimes \nu p_{3/2}$), (b) 6^+ ($\pi h_{9/2} \otimes \nu f_{5/2}$), (c) 7^+ ($\pi h_{9/2} \otimes \nu f_{5/2}$), and (d) 10^- ($\pi h_{9/2} \otimes \nu i_{13/2}$) states of the odd-$N$ astatine (red triangles, present work), bismuth (black circles) [62,79], and francium (blue squares) [61,80,81] isotopes. The filled and hollow data points represent the ground and isomeric states, respectively. The dashed lines represent values for the astatine isotopes, calculated using the additivity relation.

3. Even-A astatine isotopes

The magnetic moments of the even-A astatine states with $I^\pi = 3^+, 6^+, 7^+$, and 10^- are plotted in Figs. 10(a), 10(b) 10(c), and 10(d), respectively, along with those of the states with matching spins and parities in francium and bismuth isotopes. In all cases, the values of μ for astatine nuclei follow the trends observed in the bismuth and francium states of the same spin and parity.

The discussion of the magnetic moments of the even-A astatine isotopes will be guided by comparisons with estimations from the additivity relation [39] to obtain information on the underlying configurations. According to the additivity relation, the magnetic moment of a two-particle state in an odd-odd nucleus with spin I can be calculated using the following formula:

$$\mu_{\rm add} = \frac{I}{2}\left(\frac{\mu_p}{i_p} + \frac{\mu_n}{i_n}\right) + \frac{I}{2}\left(\frac{\mu_p}{i_p} - \frac{\mu_n}{i_n}\right)\frac{i_p(i_p+1) - i_n(i_n+1)}{I(I+1)}, \quad (13)$$

where the subscripts p and n denote the odd proton and neutron, respectively; i is the single-particle angular momenta; and μ_p, μ_n are the single-particle magnetic moments. The values of μ_p were taken to be equal to the magnetic moments of neighboring even-N astatine isotopes, such that $\mu_p({\rm At}_N) = \mu({\rm At}_{N+1})$. Similarly, the magnetic moments of the adjacent odd-N polonium nuclei were used for μ_n, giving $\mu_n({\rm At}_N) = \mu({\rm Po}_N)$.

Calculations by the additivity relation were performed with the following configuration assignments: $I^\pi = 3^+ : (\pi h_{9/2} \otimes \nu p_{3/2})$; $I^\pi = 6^+ : (\pi h_{9/2} \otimes \nu f_{5/2})$; $I^\pi = 7^+ : (\pi h_{9/2} \otimes \nu f_{5/2})$; $I^\pi = 10^- : (\pi h_{9/2} \otimes \nu i_{13/2})$.

In almost all cases, the magnetic moments are well described by the additivity relation (see Fig. 10). For $^{210}{\rm At}_{125}$ (not shown in Fig. 10), $\mu_{\rm exp}(5^+) = 4.74(12)\ \mu_N$ and $\mu_{\rm add}(5^+; \pi h_{9/2} \otimes \nu p_{1/2}) = 4.82 \mu_N$. This agreement between the experimental values and those calculated using the additivity relation testifies to the purity of the assigned configurations.

It is worth noting that the decrease of $\mu(3^+)$ when going from $N = 115$ to $N = 111$ is connected by the additivity relation with the increase of the magnetic moment of the $3/2^+$ isotonic polonium states [$\mu(^{199}{\rm Po}_{115}) = -0.912(65)\mu_N$; $\mu(^{195}{\rm Po}_{111}) = -0.601(42)\mu_N$]. This increase was explained in Ref. [7] as the result of the gradual increase in deformation of the corresponding polonium isotopes. Thus, the behavior of the magnetic moments for the 3^+ states in astatine isotopes may also be related to a similar deformation change.

The only case for which the experimental results are not well described by the additivity rule is ^{206}At ($N = 121$), when presuming an $I = 5$ spin assignment [82]. Under this assumption, $\mu_{\rm add}(5^+)$ differs markedly from the experimental value obtained for ^{206}At: $\mu_{\rm add}(5^+; \pi h_{9/2} \otimes \nu f_{5/2}) = 3.89 \mu_N$, $\mu_{\rm exp}(5^+) = 4.34(12)\ \mu_N$. A possible admixture from a ($\pi h_{9/2} \otimes \nu p_{3/2}$) configuration would lead to the even larger discrepancy between the experimental and calculated values, as $\mu_{\rm add}(5^+; \pi h_{9/2} \otimes \nu p_{3/2}) = 3.44 \mu_N$. However, $\mu_{\rm add}(6^+; \pi h_{9/2} \otimes \nu f_{5/2}) = 4.39 \mu_N$ is in good agreement with $\mu_{\rm exp}(6^+) = 4.39(13)\ \mu_N$ [see Fig. 10(b)].

The previous $I = 5$ assignment for $^{206}{\rm At}^g$ was based upon the observed β-decay feeding to the 4^+ and 6^+ states in ^{206}Po, with nearly equal $\log ft$ values [82]. In contrast, our additivity-relation analysis would support an $I = 6$ spin assignment for the ground state of ^{206}At. Such an assignment was also proposed in Ref. [83], in which the hindrance factor of the $^{210}{\rm Fr}(I = 6) \rightarrow {}^{206}{\rm At}\,\alpha$ decay was found to be surprisingly small ($HF_\alpha = 2.1$) for a decay connecting states of different spins (6^+ to 5^+). As one of the possible explanations, the authors of Ref. [83] suggested that the ground state of ^{206}At has $I^\pi = 6^+$, while the low-lying levels at 6 and 31 keV are similar to the 5^+ and 4^+ states in the ^{204}Bi isotone, respectively.

B. Quadrupole moments

1. Odd-A isotopes

The increase in collectivity when going away from the closed shell is reflected in the increase of the absolute values of Q_S (see Table II). For well-deformed axially symmetric nuclei, the quadrupole moment can be related to the quadrupole deformation parameter, via the relation

$$Q_S = \frac{I(2I-1)}{(I+1)(2I+3)}\frac{3e}{\sqrt{5\pi}} Z R_0^2 \beta_Q \left(1 + \frac{1}{7}\sqrt{\frac{20}{\pi}}\beta_Q + \cdots\right), \quad (14)$$

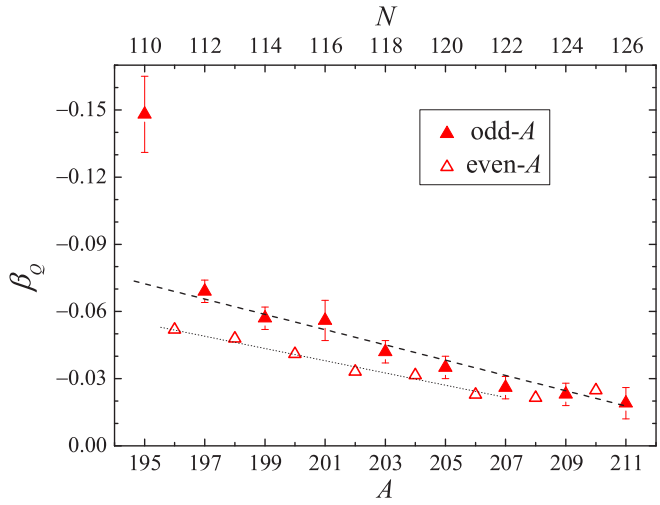

FIG. 11. Quadrupole deformation parameters calculated using Eq. (14), for odd- (filled symbols) and even-N (hollow symbols) ground states of astatine nuclei. For $A = 195$, the $7/2^-$ isomeric state is shown. The dashed lines are to guide the eye only.

where β_Q represents the deformation parameter extracted from the value of Q_S and $R_0 = 1.2 \times A^{1/3}$. However, as was shown in Ref. [39] and references therein, it is also instructive to use this relation for nuclei with small deformations. The values of β_Q extracted using this formula give an insight into the development of collectivity (note that in Ref. [39], Eq. (14) was applied to nuclei with $N = 116 - 126$ at $\beta_Q \approx 0.05$, in particular to ^{211,209}At).

The values of β_Q extracted using Eq. (14) for the ground states of the odd-A $I = 9/2$ and the even-A astatine nuclei are shown in Fig. 11 (for $A = 195$, the isomeric $I^\pi = 7/2^-$ state is shown). The values of β_Q vary linearly (from -0.02 to -0.07) as the neutron number decreases away from the $N = 126$ closed neutron shell, until $N = 112$. This gradual change is interrupted by a sudden increase in deformation (from -0.07 to -0.15) between ^{197}At^g and ^{195}At^m. A similar dramatic change in the deformation from 0.10 to -0.21 was theoretically predicted between ^{199}At and ^{198}At in Ref. [84], using the microscopic-macroscopic (MM) calculations with the finite-range droplet model.

A comparison between the deformation parameters extracted from the IS data and those from the Q_S values will be presented in Sec. V C 1.

2. Even-A isotopes

The even-A astatine nuclei were analyzed in the framework of the "quadrupole additivity rule". The additivity rule for magnetic moments, discussed in Sec. V A 3, is the simplest case of a general tensor coupling scheme. In the case of the spectroscopic quadrupole moments, it can be represented as follows (see Ref. [85] and references therein):

$$Q_S^{\rm add} = q_p Q_S(j_p) + q_n Q_S(j_n), \tag{15}$$

with the spectroscopic quadrupole moments $Q_S(j_{p,n})$ of the single-particle proton and neutron states with angular momenta

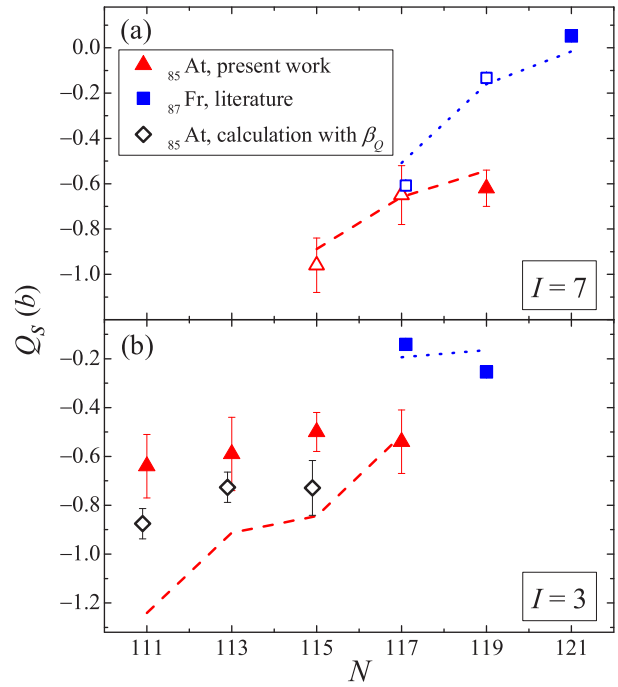

FIG. 12. Comparison of $Q_S^{\rm add}$ and $Q_S^{\rm exp}$ for isotopes of astatine (red triangles) and francium (blue squares) with (a) $I = 7\,(\pi h_{9/2} \otimes \nu f_{5/2})$ and (b) $I = 3\,(\pi h_{9/2} \otimes \nu p_{3/2})$. The filled symbols indicate ground states and the hollow ones indicate isomeric states. Results of the calculations using the quadrupole additivity rule [Eq. (15)] are indicated by the red-dashed and blue-dotted lines for the astatine and francium isotopes, respectively. The black diamonds in panel (b) represent calculations made using Eq. (14), with β_Q taken from the Q_S value of the adjacent even-N At.

$j_{p,n}$ and

$$q_i = (-1)^{j_p + j_n + I}(2I+1)\begin{Bmatrix} j_p & j_n & I \\ a & b & j_i \end{Bmatrix} \times \begin{pmatrix} I & I & 2 \\ I & -I & 0 \end{pmatrix}\begin{pmatrix} j_i & j_i & 2 \\ j_i & -j_i & 0 \end{pmatrix}^{-1}, \tag{16}$$

where $\{\cdots\}$ and $(\cdots)$ are the Wigner $6j$ and $3j$ symbols, respectively (see Ref. [86]); $i = p$ or n; $a = I$, $b = 2$ for $j_i = j_p$; and $a = 2, b = I$ for $j_i = j_n$.

This quadrupole additivity rule was tested by calculating Q_S for even-A francium and astatine isotopes with spins $I = 3\,(\pi h_{9/2} \otimes \nu p_{3/2})$ and $I = 7\,(\pi h_{9/2} \otimes \nu f_{5/2})$. For $Q_S(j_n)$, the experimental quadrupole moments of the adjacent even-Z, odd-N isotopes were used: $Q_S(_{86}\mathrm{Rn}_N)$ [68] for $_{87}\mathrm{Fr}_N$, and $Q_S(_{84}\mathrm{Po}_N)$ [7,87] for $_{85}\mathrm{At}_N$. Similarly, the experimental quadrupole moments of the adjacent even-N francium [61,81] and astatine (present work) isotopes were used for the values of $Q_S(j_p)$. In cases where no experimental data were available, interpolation or extrapolation was applied.

The values of Q_S calculated using the quadrupole additivity rule are in good agreement with the experimental data for astatine and francium nuclei with $I = 6$, 7, 10 [see Fig. 12(a) for nuclei with $I = 7$; the results for $I = 6$, 10 are not

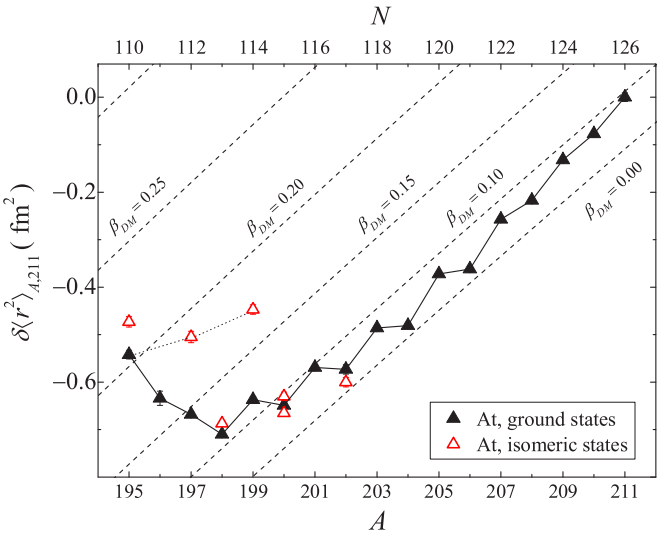

FIG. 13. Changes in mean-square charge radii for the astatine isotopes, compared with the predictions of the droplet model (parameters taken from Ref. [69]) for various deformations. The solid line connects the data points for the ground states in astatine isotopes and the dotted line does the same for ground or isomeric states with $I = 1/2$.

shown here]. In contrast, the same calculations completely fail to describe the Q_S(At, $I = 3$) with a $(\pi h_{9/2} \otimes \nu p_{3/2})$ configuration [see Fig. 12(b)]. This may be related to the marked increase in deformation at $N < 113$ (see discussion of radii in Sec. V C). The quadrupole additivity rule stemming from the spherical shell-model approach does not work for deformed nuclei (cf. corresponding modification of the magnetic-moment additivity rule in the case of deformation [88]). When the astatine isotopes with $N < 113$ are assumed to be deformed, one may estimate the expected quadrupole moments for the 3^+ states using Eq. (14), with β_Q taken from the Q_S of the adjacent even-N astatine nuclei. As is seen in Fig. 12(b), the corresponding Q_S calculated using β_Q values of neighboring isotopes agrees much better with experiment than those predicted by the quadrupole additivity rule. Thus, the observed discrepancy with the additivity rule prediction supports the proposed onset of deformation in astatine nuclei at $N < 113$.

C. Charge radii

1. Ground states

The changes in mean-square charge radii, extracted using Eq. (8), are shown in Fig. 13. After a near-linear decrease between $N = 126$ and $N = 114$, the $\delta\langle r^2\rangle$ values are observed to increase, starting at ^{198}At($N = 113$). This increase continues as the neutron number decreases further, with ^{195}At seen to have almost the same charge radius as ^{203}At, despite the former having eight fewer neutrons. Correspondingly, the mean-square deformation, β_{DM} [see Eq. (12)], remains nearly constant and small (0.07–0.10) in $^{200-211}$At, but increases rapidly for $N < 115$, to a maximum of $\beta_{DM} = 0.21$ for ^{195}At$_{110}$ (see Table II).

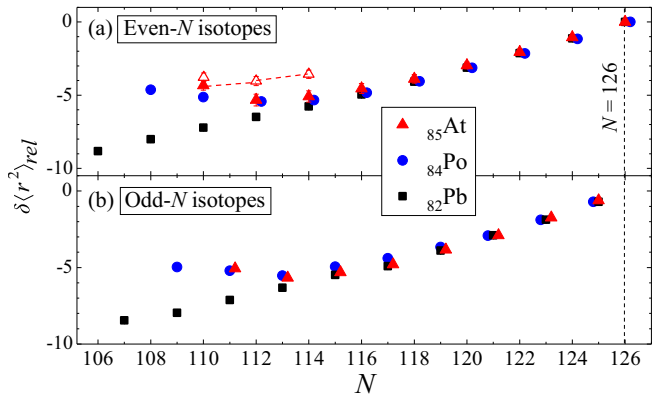

FIG. 14. Comparison of relative radii for astatine ground states (red triangles) and isomers (red hollow triangles), with polonium (blue circles) [64,70,87] and lead (black squares) [6,89,90] isotopes. For clarity, the odd- and even-A isotopes are plotted separately, in order to remove the effects of the odd-even staggering. The dashed red line connects the data points for the $I = 1/2$ states in astatine.

It is instructive to use relative $\delta\langle r^2\rangle$ values to compare the different isotopic chains in the lead region. This normalization has the benefit of removing the indeterminacy of the electronic factors. The relative value of $\delta\langle r^2\rangle$ is defined as

$$\delta\langle r^2\rangle_{\rm rel} = \frac{\delta\langle r^2\rangle_{N,126}}{\delta\langle r^2\rangle_{124,122}}. \tag{17}$$

Figure 14 shows the changes in $\delta\langle r^2\rangle_{\rm rel}$ for the lead, polonium and astatine nuclei. The IS data from Refs. [64,70,87] and Refs. [6,89,90] were used for the polonium and lead nuclei, respectively.

As seen in Fig. 14, the ground states of astatine isotopes perfectly follow the N dependence of the relative radii for polonium nuclei with $N > 110$. However, both isotopic chains deviate from the nearly spherical lead trend at $N < 115$. In the case of the polonium nuclei, this deviation was attributed to an onset of deformation [64].

The systematics of low-lying states in polonium isotopes are remarkably similar to those of the corresponding astatine nuclei. In particular, a drop in the excitation energy of the 2^+ states when going from ^{200}Po to ^{198}Po and a bigger decrease between ^{198}Po and ^{196}Po are analogous to the behavior observed for $11/2^-$ and $13/2^-$ states in ^{201,199,197}At (see Refs. [15,75] and references therein). These reductions in state energies have been interpreted as evidence for an increase in collectivity and an onset of deformation in the even-even polonium core. Due to the similarity between the polonium and astatine nuclei, the same increase in collectivity was proposed to occur around ^{197}At [76]. This conclusion is supported by the resemblance in the behavior of astatine and polonium radii between $N = 111$ and $N = 126$, presented in this work.

The results from two experiments, one a lifetime measurement [91] and the other a Coulomb excitation study [92], indicate that the ground state in ^{196}Po exhibits a mixing of spherical and weakly deformed oblate structures. Analysis of radii and electromagnetic moments enables the extension of this interpretation to ^{192,193,194,195}Po [7,64,70]. The increase

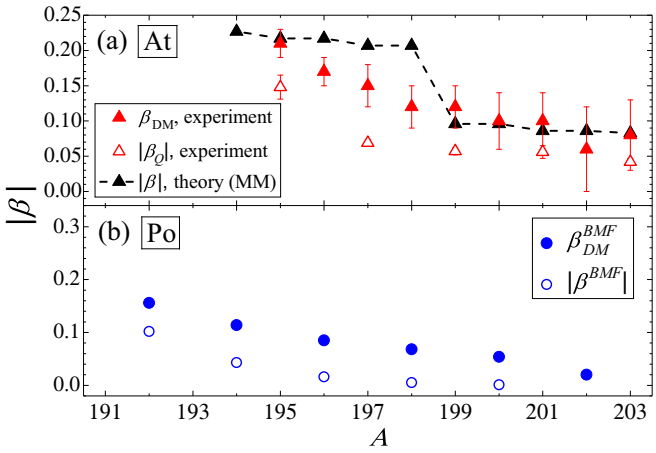

FIG. 15. (a) Comparison of experimental mean-square deformation for At isotopes. The filled red triangles represent values of β_{DM} [see Eq. (12)], the hollow red triangles are values for β_Q [deformation extracted from Q_S, see Eq. (14)], and the filled black triangles are the predictions of the MM [84]. (b) Comparison of β_{DM}^{BMF} (filled circles), and β^{BMF} (hollow circles), calculated using the BMF method for the even-even polonium isotopes [100]. The values of β_{DM}^{BMF} may be regarded as theoretical estimations of experimental β_{DM} values, and β^{BMF} as theoretical estimations of β_Q.

in mixing of oblate and nearly spherical configurations in the ground states of the light even-A polonium isotopes is confirmed by in-beam and α-decay data [93,94]. Similar to the even-A polonium nuclei, the decay pattern of odd-mass ^{193,195}Po^{m,g} is also understood as a result of the mixing of the deformed (oblate) and the spherical configurations (see Refs. [95,96] and references therein). Keeping in mind this similarity between astatine and polonium nuclei, one can extend this configuration-mixing interpretation to the structure of the light astatine nuclei.

Theoretical models based on the mean-field approach (MM or Hartree-Fock models) which do not account for configuration mixing are unable to reproduce the rapid but smooth radii increase for polonium and astatine nuclei with $N < 115$. In Fig. 15(a), experimental β_{DM}(At) values [extracted using Eq. (12)], are compared with the results of the MM calculations [84], which predict a sudden increase in deformation between ^{199}At and ^{198}At. Such behavior is not observed in the experimental data, which shows a gradual increase. A similar sudden increase is predicted between ^{194}At and ^{195}At, by Hartree-Fock-Bogoliubov calculations using the Gogny D1S interaction [97,98]. In both models, the potential energy surface for the neutron-deficient astatine isotopes has several minima with nearly identical depth (see also Ref. [99]). Correspondingly, it is natural to suppose that for these nuclei mixing takes place between configurations of different deformations. The aforementioned experimental observations support this supposition.

This mixing can be taken into account in the beyond-mean-field (BMF) approach, which combines projection techniques with the generator coordinate method (GCM). Mean-field wave functions are constructed by Hartree-Fock-BCS calculations. They are then projected on angular momentum and particle number to form a basis of states that are mixed by the GCM (see Ref. [100] and references therein). This model, at least qualitatively, describes the unusual radii (deformation) trend for the even-even polonium isotopes at $N < 115$ [64,100].

At $N = 110$ (^{195}At, ^{194}Po), the increase in the radius of ^{195}At$_{110}$ (especially for $7/2^-$ isomer) in comparison with ^{192}Pb$_{110}$ is evidently larger than that of ^{194}Po$_{110}$ [see Fig. 14(a)]. This increase in radius (deformation) possibly points to a change in structure of ^{195}At compared to ^{194}Po, whereas heavier astatine isotopes remain similar to their polonium cores.

A sharp increase in the quadrupole moment and β_Q is observed when going from $A = 196$ to $A = 195$ (see Fig. 11). In contrast to this, a smooth behavior is seen in the mean-square deformation, β_{DM} [see Eq. (12)], with no irregularities observed at $A = 195$ [see Fig. 15(a)]. The values of β_{DM} in nuclei with $N < 115$ ($A < 200$), i.e., exactly after the presumed onset of deformation, is noticeably larger than the deformation parameter β_Q [see Fig. 15(a)]. This discrepancy may be qualitatively explained in the framework of the BMF approach. Although within the configuration-mixing BMF method one cannot assign an intrinsic deformation to the wave functions, it is the well-defined mean deformation β^{BMF} that may "play the role" of intrinsic deformation and determine the Q_S value [by Eq. (14)]. By using Eq. (12) with the values of $\delta\langle r^2\rangle$ calculated using the BMF approach, one can estimate the mean-square deformation. In Fig. 15(b), the mean-square deformation parameter, β_{DM}^{BMF}, is compared with the mean-deformation parameter, β^{BMF}, for isotonic polonium nuclei (data are taken from Ref. [100]). Although theory noticeably underestimates the absolute values of β_{DM}, it qualitatively explains the observed discrepancy between β_Q and β_{DM} by the spread of the collective wave function in deformation space.

2. $1/2^+$ states

Three $1/2^+$ states have been studied in the present work: the intruder isomers ^{197,199}At^m and ^{195}At^g. The $I^\pi = 1/2^+$ intruder states in ^{197,199}At^m are seen to have a larger radius than the corresponding normal $I^\pi = 9/2^-$ states, which substantiates the interpretation that these are shape-coexisting states.

In Figs. 13 and 14, the radii of the $1/2^+$ states in astatine are seen to lie on a straight line, with no irregularity seen where the $1/2^+$ state becomes the ground state, at $A = 195$. A consistent picture is observed in the magnetic moments, namely, $\mu(^{195}\text{At}; 1/2^+)$ agrees within the limits of uncertainties with the magnetic moments of ^{197,199}At^m [see Fig. 9(b)]. Therefore, it is unlikely that ^{195}At^g has a different nature to ^{197,199}At^m due to the presumed admixture of a deformed $1/2^+$ state associated with a prolate $1/2^+[660]$ Nilsson orbital (see Ref. [71], where this assumption was applied to bismuth nuclei to explain the continuing downward trend of the excitation energies of the $1/2^+$ states). The same conclusion may be drawn from the fair agreement of μ between astatine and thallium nuclei [see Fig. 9(b) and related discussion]. Thus, the disappearance of the parabolic trend inherent to intruder-isomer excitation energies [10] is more likely connected to the change in structure of the $9/2^-$ ground states of astatine isotopes with $N < 115$, rather than an oblate-prolate mixture in the $1/2^+$ states.

VI. CONCLUSIONS

Hyperfine structure parameters and isotope shifts have been measured in the astatine isotopic chain for $^{195-211}$At, using the 216- and 795-nm atomic transitions. Magnetic and quadrupole moments and changes in the nuclear mean-square charge radii have been deduced using the results of large-scale atomic calculations. The opportunity to assess the reliability of these calculations and their ascribed uncertainties was presented by their comparison with systematics.

For the first time, the MR-TOF MS device was used to perform hfs and IS measurements. The use of the device allowed the study of isotopes that would otherwise be inaccessible using the standard RILIS approach, due to their long half-lives, or the strong presence of surface ionized isobaric contamination. Although in this study the MR-TOF MS was used for measurements of long-lived isotopes, its application is not limited to these cases; previous studies have measured masses of isotopes with $T_{1/2} < 50$ ms, and production rates as low as 10 ions per second [101].

For the $9/2^-$ odd-A astatine ground states, a linear decrease of the magnetic moment value with the decrease of A has been observed. This decrease is similar to the corresponding behavior seen for $\mu(9/2^-)$ in the bismuth and francium isotopes. The application of the additivity relation for the magnetic moments of even-A astatine nuclei confirms their leading configuration assignments and spins. The additivity relation holds for all but ^{206}At, where a spin-parity assignment of $I^\pi = 6^+$ is proposed, based on the better agreement with the additivity-relation calculation.

The additivity rule for the quadrupole moments of even-A astatine and francium nuclei has been applied. It has been shown that this rule describes Q_S(At) for spherical nuclei fairly well. The failure of the rule in describing the quadrupole moments for $I = 3$ At isotopes with $N < 115$ indicates a possible onset of deformation in these nuclei.

The charge radii of the astatine ground states follow the trend previously observed in isotonic polonium nuclei. Similar to the polonium case, the strong deviation of $\delta\langle r^2\rangle$ for astatine from the trend of the (spherical) lead isotopes for $N < 115$ is interpreted as an onset of deformation. A significant difference in charge radii for ground and isomeric (intruder, $1/2^+$) states in ^{197,199}At is observed. The magnetic moment of ^{195}At^g ($I^\pi = 1/2^+$) is in good agreement with those of ^{197}At^m and ^{199}At^m, within the limits of experimental uncertainties. This agreement between the $\mu(I = 1/2)$ values may indicate that all three possess the same structure.

The marked increase of the mean-square charge radius of ^{195}At^m ($I^\pi = 7/2^-$), in comparison with isotonic ^{194}Po, has been interpreted as a structural change; ^{195}At^m is assumed to be strongly oblate deformed, whereas the ground state of ^{194}Po represents an admixture of deformed and spherical configurations with a relatively small mean deformation. This interpretation is supported by the magnetic and quadrupole moment measurement. The rapid change in Q_S when going from ^{197}At to ^{195}At^m can be explained by the corresponding increase in the mean deformation. The $\mu(^{195}\text{At}^m)$ is well described with the assumption of the odd proton predominantly occupying a $7/2^-[514]$ Nilsson orbital, at a sizable oblate deformation.

The noticeable difference between the mean-square deformation deduced from the IS data and deformation evaluated by Q_S analysis, is proposed to result from the difference between $\langle\beta_2^2\rangle^{1/2}$ and the mean deformation, due to the spread of the collective wave function in deformation space. This effect has been shown to be qualitatively described by the BMF model.

ACKNOWLEDGMENTS

We would like to acknowledge the support of the ISOLDE Collaboration and technical teams. This work has been funded by FWO-Vlaanderen (Belgium), by GOA/2010/010 (BOF KU Leuven), by the Interuniversity Attraction Poles Programme initiated by the Belgian Science Policy Office (BriX network P7/12), by the European Union's Seventh Framework Programme for Research and Technological Development under Grant Agreements No. 262010 (ENSAR), No. 267194 (COFUND), and No. 289191 (LA^{3}NET), by a grant from the European Research Council (Grant No. ERC-2011-AdG-291561-HELIOS), by grants from the U.K. Science and Technology Facilities Council, by the Slovak Research and Development Agency (Contract No. APVV-14-0524) and the Slovak Grant Agency VEGA (Contract No. 1/0532/17), by the Max-Planck Society, by the Bundesministerium für Bildung und Forschung under Contracts No. 05P15HGCIA, No. 05P12HGCI1, No. 05P12HGFNE, No. 05P09ODCIA, and No. 05P15SJCIA, and by the French IN2P3. S.K. acknowledges support from the Robert-Bosch Foundation, T.E.C. was supported by a U.K. Science and Technology Facilities Council Ernest Rutherford Fellowship (ST/J004189/1). Research was funded by a Ph.D. grant of the Agency for Innovation by Science and Technology (IWT). The atomic calculations were carried out with the supercomputer Deszno purchased thanks to the financial support of the European Regional Development Fund in the framework of the Polish Innovation Economy Operational Program (Contract No. POIG.02.01.00-12-023/08).

APPENDIX: PROCEDURE FOR FITTING THE HFS DATA

The experimental hfs spectra were fitted with a convolution of a Gaussian Doppler profile N_G to describe the thermal distribution of atomic velocities corresponding to the ion source temperature and P_{ion}, representing the probability of photoionization, which depends upon the spectral density of the laser power. In a general form, the number of photoionized atoms for an individual hfs transition can be presented as

$$N_{\text{ion}}(\nu) = N_0 \int N_G(\nu') P_{\text{ion}}(\nu - \nu') d\nu'. \tag{A1}$$

In a simple case (two-step photoinization scheme, well-resolved hfs components, absence of saturation of all transitions), the photoionization probability, P_{ion}, is proportional to the spectral density of the laser power I_L, and can be presented as

$$P_{\text{ion}}(\nu - \nu') \propto \sum S_{FF'} I_L(\nu + \Delta\nu^{FF'} - \nu'), \tag{A2}$$

where $S_{FF'}$ is the relative probability of the transition [4]:

$$S_{FF'} \propto (2F+1)(2F'+1)\begin{Bmatrix} J' & F' & I \\ F & J & 1 \end{Bmatrix}^2. \quad \text{(A3)}$$

The intensity of hfs components calculated using Eq. (A2) and those observed experimentally can differ significantly (see Figs. 4 and 5). This is due to saturation effects and a finite spectral width of the broadband laser radiation (as well as its frequency detuning from the hfs centroid). To take into account the saturation of transitions, pumping processes between hfs structure components and population redistribution in the hfs levels, the number of photo ions for each frequency step ν' in the integration of Eq. (A1) was calculated by solving the rate equations for all hfs sublevels of all states in a given photoionization scheme in a way similar to that in our previous work (see details in Ref. [7]). To take into account the saturation effect for polarized laser radiation more accurately, all sublevels with different magnetic quantum number, M_F $|F,M_F\rangle$, were included into the equations system. In this approach, the relative probabilities, W, of $|F,M_F\rangle \rightarrow |F',M'_F\rangle$ transitions are proportional to

$$W(M_F,F;M'_F,F') \propto S'(M_F,F;M'_F,F')I_L(\nu+\Delta\nu^{FF'}-\nu'), \quad \text{(A4)}$$

with the relative probability of single-photon absorption S' defined as

$$S'(M_F,F;M'_F,F') \propto (2F+1)(2F'+1) \begin{pmatrix} F & 1 & F' \\ -M_F & Q & M'_F \end{pmatrix}^2 \begin{Bmatrix} J' & F' & I \\ F & J & 1 \end{Bmatrix}^2, \quad \text{(A5)}$$

where $Q = M_F - M'_F = 0,\pm 1$. For linear polarization, only transitions with $\Delta M_F = 0$ are possible.

For the narrowband Ti:Sa laser, a set of equidistant resonator modes with a Gaussian distribution of intensities I_L was used. Line-shape parameters for I_L were taken from Ref. [102]. For the dye laser, a single Lorentzian line profile was used. The width of hyperfine structure for the $\lambda_1 = 216$-nm, and $\lambda_2 = 795$-nm transitions was $\approx$20 GHz (see Figs. 4 and 5). The spectral width of the broadband lasers used for excitation of the corresponding transitions is large. For example, the observed bandwidth of the broadband dye laser was $\approx$30–40 GHz after frequency tripling. Nevertheless, the finite linewidth and especially the frequency detuning of the nonscanned broadband laser from the hfs resonance position can distort the relative intensities of the individual components across the hfs. To take this into account, the spectral density of the broadband laser radiation was represented with a Lorentzian profile, with line-shape parameters based on the experimentally observed profiles. The linewidth and frequency detuning from the resonance position of this laser can be fixed or left as a free parameter in the fitting procedure.

[1] S. Rothe *et al.*, Nat. Commun. **4**, 1835 (2013).
[2] S. Raeder, J. Lassen, H. Heggen, and A. Teigelhöfer, Hyperfine Interact. **227**, 77 (2014).
[3] R. McLaughlin, J. Opt. Soc. Am. **54**, 965 (1964).
[4] P. Campbell, I. D. Moore, and M. R. Pearson, Prog. Part. Nucl. Phys. **86**, 127 (2016).
[5] R. N. Wolf *et al.*, Int. J. Mass Spectrom. **349**, 123 (2013).
[6] H. DeWitte, A. N. Andreyev, N. Barre, M. Bender, T. E. Cocolios, S. Dean, D. Fedorov, V. N. Fedoseyev, L. M. Fraille, S. Franchoo *et al.*, Phys. Rev. Lett. **98**, 112502 (2007).
[7] M. D. Seliverstov, T. E. Cocolios, W. Dexters, A. N. Andreyev, S. Antalic, A. E. Barzakh, B. Bastin, J. Buscher, I. G. Darby, D. V. Fedorov *et al.*, Phys. Rev. C **89**, 034323 (2014).
[8] H. Kettunen *et al.*, Eur. Phys. J. A **16**, 457 (2003).
[9] H. Kettunen *et al.*, Eur. Phys. J. A **17**, 537 (2003).
[10] E. Coenen, K. Deneffe, M. Huyse, P. Van Duppen, and J. L. Wood, Phys. Rev. Lett. **54**, 1783 (1985).
[11] E. Coenen, K. Deneffe, M. Huyse, P. Van Duppen, and J. L. Wood, Z. Phys. A **324**, 485 (1986).
[12] K. Andgren, U. Jakobsson, B. Cederwall, J. Uusitalo, T. Back, S. J. Freeman, P. T. Greenlees, B. Hadinia, A. Hugues, A. Johnson *et al.*, Phys. Rev. C **78**, 044328 (2008).
[13] U. Jakobsson, S. Juutinen, J. Uusitalo, M. Leino, K. Auranen, T. Enqvist, P. T. Greenlees, K. Hauschild, P. Jones, R. Julin *et al.*, Phys. Rev. C **87**, 054320 (2013).
[14] K. Auranen, J. Uusitalo, S. Juutinen, U. Jakobsson, T. Grahn, P. T. Greenlees, K. Hauschild, A. Herzan, R. Julin, J. Konki *et al.*, Phys. Rev. C **90**, 024310 (2014).
[15] K. Auranen, J. Uusitalo, S. Juutinen, H. Badran, F. D. Bisso, D. Cox, T. Grahn, P. T. Greenlees, A. Herzan, U. Jakobsson *et al.*, Phys. Rev. C **95**, 044311 (2017).
[16] NNDC, Evaluated Nuclear Structure Data File (September 2017), http://www.nndc.bnl.gov/ensdf/.
[17] R. Catherall *et al.*, J. Phys. G: Nucl. Part. Phys. **44**, 094002 (2017).
[18] G. D. Alkhazov *et al.*, Nucl. Instrum. Methods B **69**, 517 (1992).
[19] B. A. Marsh *et al.*, Nucl. Instrum. Methods B **317**, 550 (2013).
[20] V. I. Mishin *et al.*, Nucl. Instrum. Methods B **73**, 550 (1993).
[21] V. N. Fedosseev *et al.*, J. Phys. G: Nucl. Part. Phys. **44**, 084006 (2017).
[22] S. Rothe, Ph.D. thesis, Institut für Physik Johannes Gutenberg-Universität Mainz, Germany, 2013 (unpublished).
[23] R. N. Wolf *et al.*, Phys. Rev. Lett. **110**, 041101 (2013).
[24] F. Herfurth *et al.*, Nucl. Instrum. Methods A **469**, 254 (2001).
[25] F. Wienholtz *et al.*, Nature (London) **498**, 346 (2013).
[26] D. Atanasov, P. Ascher, K. Blaum, R. B. Cakirli, T. E. Cocolios, S. George, S. Goriely, F. Herfurth, H. T. Janka, O. Just *et al.*, Phys. Rev. Lett. **115**, 232501 (2015).
[27] A. Welker, N. A. S. Althubiti, D. Atanasov, K. Blaum, T. E. Cocolios, F. Herfurth, S. Kreim, D. Lunney, V. Manea, M. Mougeot *et al.*, Phys. Rev. Lett. **119**, 192502 (2017).
[28] M. Rosenbusch *et al.*, Appl. Phys. B **114**, 147 (2014).
[29] F. Wienholtz *et al.*, Phys. Scr. **T166**, 014068 (2015).
[30] B. A. Marsh *et al.*, Hyperfine Interact. **227**, 101 (2014).
[31] A. E. Barzakh, D. V. Fedorov, V. S. Ivanov, P. L. Molkanov, F. V. Moroz, S. Y. Orlov, V. N. Panteleev, M. D. Seliverstov, and Y. M. Volkov, Phys. Rev. C **94**, 024334 (2016).

[32] K. M. Lynch, T. E. Cocolios, J. Billowes, M. L. Bissell, I. Budincevic, T. Day Goodacre, R. P. deGroote, G. J. Farooq-Smith, V. N. Fedosseev, K. T. Flanagan *et al.*, Phys. Rev. C **93**, 014319 (2016)
[33] B. Cheal and K. T. Flanagan, J. Phys. G **37**, 113101 (2010).
[34] J. R. Persson, At. Data Nucl. Data Tables **99**, 62 (2013).
[35] D. Zwarts and P. W. M. Glaudemans, Z. Phys. A **320**, 487 (1985).
[36] A. P. Byrne *et al.*, Nucl. Phys. A **448**, 137 (1986).
[37] D. J. Decman, H. Grawe, H. Kluge, and K. H. Maier, Z. Phys. A **310**, 55 (1983).
[38] D. J. Decman *et al.*, Nucl. Phys. A **436**, 311 (1985).
[39] G. Neyens, Rep. Prog. Phys. **66**, 633 (2003).
[40] R. Collister, G. Gwinner, M. Tandecki, J. A. Behr, M. R. Pearson, J. Zhang, L. A. Orozco, S. Aubin, and E. Gomez, Phys. Rev. A **90**, 052502 (2014).
[41] E. Gomez, S. Aubin, L. A. Orozco, G. D. Sprouse, E. Iskrenova-Tchoukova, and M. S. Safronova, Phys. Rev. Lett. **100**, 172502 (2008).
[42] J. R. Beene *et al.*, Hyperfine Interact. **3**, 397 (1977).
[43] H. Ingwersen, W. Klinger, G. Schatz, and W. Witthuhn, Phys. Rev. C **11**, 243 (1975).
[44] O. Häusser, T. K. Alexander, J. R. Beene, E. D. Earle, A. B. McDonald, F. C. Khanna, and I. S. Towner, Hyperfine Interact. **2**, 334 (1976).
[45] C. Granados *et al.*, Phys. Rev. C **96**, 054331 (2017).
[46] T. Yamazaki *et al.*, Phys. Rev. Lett. **25**, 547 (1970).
[47] I. P. Grant, *Relativistic Quantum Theory of Atoms and Molecules: Theory and Computation* (Springer, New York, 2007).
[48] P. Jönsson, G. Gaigalas, J. Bieroń, C. Froese Fischer, and I. P. Grant, Comput. Phys. Commun. **184**, 2197 (2013).
[49] I. P. Grant, Comput. Phys. Commun. **84**, 59 (1994).
[50] K. G. Dyall, I. P. Grant, C. T. Johnson, F. A. Parpia, and E. P. Plummer, Comput. Phys. Commun. **55**, 425 (1989).
[51] B. J. McKenzie, I. P. Grant, and P. H. Norrington, Comput. Phys. Commun. **21**, 233 (1980).
[52] J. Bieroń, C. Froese Fischer, S. Fritzsche, G. Gaigalas, I. P. Grant, P. Indelicato, P. Jönsson, and P. Pyykkö, Phys. Scr. **90**, 054011 (2015).
[53] L. Radžiūtė, G. Gaigalas, P. Jönsson, and J. Bieroń, Phys. Rev. A **90**, 012528 (2014).
[54] J. Bieroń, C. Froese Fischer, P. Indelicato, P. Jönsson, and P. Pyykkö, Phys. Rev. A **79**, 052502 (2009).
[55] J. Bieroń, P. Jönsson, and C. Froese Fischer, Phys. Rev. A **60**, 3547 (1999).
[56] H. Yakobi, E. Eliav, L. Visscher, and U. Kaldor, J. Chem. Phys. **126**, 054301 (2007).
[57] H. Kopferman, *Nuclear Moments* (Academic Press, New York, 1958).
[58] A. de Shalit and I. Talmi, *Nuclear Shell Theory* (Academic Press, New York, 1963).
[59] R. Ferrer *et al.*, Nat. Commun. **8**, 14520 (2017).
[60] H. Grawe (unpublished).
[61] A. Coc *et al.*, Phys. Lett. B **163**, 66 (1985).
[62] M. R. Pearson *et al.*, J. Phys. G **26**, 1829 (2000).
[63] G. Fricke and K. Heilig, *Nuclear Charge Radii* (Springer, Berlin, 2004).
[64] T. E. Cocolios, W. Dexters, M. D. Seliverstov, A. N. Andreyev, S. Antalic, A. E. Barzakh, B. Bastin, J. Buscher, I. G. Darby, D. V. Fedorov *et al.*, Phys. Rev. Lett. **106**, 052503 (2011).
[65] B. Cheal, T. E. Cocolios, and S. Fritzsche, Phys. Rev. A **86**, 042501 (2012).
[66] E. Eliav, S. Fritzsche, and U. Kaldor, Nucl. Phys. A **944**, 518 (2015).
[67] S. Fritzsche, Comput. Phys. Commun. **183**, 1525 (2012).
[68] E. W. Otten, in *Nuclear Radii and Moments of Unstable Isotopes*, Treatise on Heavy Ion Science, edited by D. A. Bromley, Vol. 8 (Springer, Boston, MA, 1989), Chap. 7, pp. 517–638.
[69] D. Berdichevsky and F. Tondeur, Z. Phys. A **322**, 141 (1985).
[70] M. D. Seliverstov *et al.*, Phys. Lett. B **719**, 362 (2013).
[71] J. C. Batchelder *et al.*, Eur. Phys. J. A **5**, 49 (1999).
[72] C. N. Davids, P. J. Woods, H. T. Penttila, J. C. Batchelder, C. R. Bingham, D. J. Blumenthal, L. T. Brown, B. C. Busse, L. F. Conticchio, T. Davinson *et al.*, Phys. Rev. Lett. **76**, 592 (1996).
[73] G. L. Poli, C. N. Davids, P. J. Woods, D. Seweryniak, M. P. Carpenter, J. A. Cizewski, T. Davinson, A. Heinz, R. V. F. Janssens, C. J. Lister *et al.*, Phys. Rev. C **63**, 044304 (2001).
[74] A. N. Andreyev, D. Ackermann, F. P. Hessberger, K. Heyde, S. Hofmann, M. Huyse, D. Karlgren, I. Kojouharov, B. Kindler, B. Lommel *et al.*, Phys. Rev. C **69**, 054308 (2004).
[75] L. A. Bernstein, J. A. Cizewski, H. Q. Jin, W. Younes, R. G. Henry, L. P. Farris, A. Charos, M. P. Carpenter, R. V. F. Janssens, T. L. Khoo *et al.*, Phys. Rev. C **52**, 621 (1995).
[76] M. B. Smith *et al.*, Eur. Phys. J. A **5**, 43 (1999).
[77] Ch. Stenzel *et al.*, Nucl. Phys. A **411**, 248 (1983).
[78] A. E. Barzakh, A. N. Andreyev, T. E. Cocolios, R. P. deGroote, D. V. Fedorov, V. N. Fedosseev, R. Ferrer, D. A. Fink, L. Ghys, M. Huyse *et al.*, Phys. Rev. C **95**, 014324 (2017).
[79] A. E. Barzakh, D. V. Fedorov, V. S. Ivanov, P. L. Molkanov, F. V. Moroz, S. Yu. Orlov, V. N. Panteleev, M. D. Seliverstov, and Yu. M. Volkov, Phys. Rev. C **95**, 044324 (2017).
[80] K. M. Lynch, J. Billowes, M. L. Bissell, I. Budincevic, T. E. Cocolios, R. P. DeGroote, S. DeSchepper, V. N. Fedosseev, K. T. Flanagan, S. Franchoo *et al.*, Phys. Rev. X **4**, 011055 (2014).
[81] A. Voss, F. Buchinger, B. Cheal, J. E. Crawford, J. Dilling, M. Kortelainen, A. A. Kwiatkowski, A. Leary, C. D. P. Levy, F. Mooshammer *et al.*, Phys. Rev. C **91**, 044307 (2015).
[82] E. W. A. Lingeman, Phys. Scr. **15**, 205 (1977).
[83] P. Kuusiniemi, F. P. Heßberger, D. Ackermann, S. Hofmann, and I. Kojouharov, Eur. Phys. J. A **23**, 417 (2005).
[84] P. Möller, A. J. Sierk, T. Ichikawa, and H. Sagawa, At. Data Nucl. Data Tables **109**, 1 (2016).
[85] J. Eberz *et al.*, Z. Phys. A **326**, 121 (1987).
[86] A. López Ariste, S. Tomczyk, and R. Casini, Astrophys. J. **580**, 519 (2002).
[87] D. Kowalewska, K. Bekk, S. Göring, A. Hanser, W. Kalber, G. Meisel, and H. Rebel, Phys. Rev. A **44**, R1442 (1991).
[88] C. Ekström, G. Wannberg, and Y. S. Shishodia, Hyperfine Interact. **1**, 437 (1975).
[89] M. Anselment, W. Faubel, S. Goring, A. Hanser, G. Meisel, H. Rebel, and G. Schatz, Nucl. Phys. A **451**, 471 (1986).
[90] M. D. Seliverstov *et al.*, Eur. Phys. J. A **41**, 315 (2009).
[91] T. Grahn, A. Dewald, P. T. Greenlees, U. Jakobsson, J. Jolie, P. Jones, R. Julin, S. Juutinen, S. Ketelhut, T. Kroll *et al.*, Phys. Rev. C **80**, 014323 (2009).
[92] N. Kesteloot *et al.*, Phys. Rev. C **92**, 054301 (2015).
[93] K. Helariutta, T. Enqvist, P. Jones, R. Julin, S. Juutinen, P. Jamsen, H. Kankaanpaa, P. Kuusiniemi, M. Leino, M. Muikku *et al.*, Phys. Rev. C **54**, R2799 (1996).

[94] K. Van de Vel, A. N. Andreyev, D. Ackermann, H. J. Boardman, P. Cagarda, J. Gerl, F. P. Hessberger, S. Hofmann, M. Huyse, D. Karlgren *et al.*, Phys. Rev. C **68**, 054311 (2003).
[95] A. N. Andreyev, M. Huyse, K. Van de Vel, P. Van Duppen, O. Dorvaux, P. Greenlees, K. Helariutta, P. Jones, R. Julin, S. Juutinen *et al.*, Phys. Rev. C **66**, 014313 (2002).
[96] K. Helariutta *et al.*, Eur. Phys. J. A **6**, 289 (1999).
[97] S. Hilaire and M. Girod, Eur. Phys. J. A **33**, 237 (2007).
[98] S. Hilaire and M. Girod, in *International Conference on Nuclear Data for Science and Technology 2007* (EDP Sciences, Les Ulis, France, 2008), p. 107.
[99] P. Möller, A. J. Sierk, R. Bengtsson, H. Sagawa, and T. Ichikawa, At. Data Nucl. Data Tables **98**, 149 (2012).
[100] J. M. Yao, M. Bender, and P.-H. Heenen, Phys. Rev. C **87**, 034322 (2013).
[101] M. Rosenbusch, P. Ascher, D. Atanasov, C. Barbieri, D. Beck, K. Blaum, C. Borgmann, M. Breitenfeldt, R. B. Cakirli, A. Cipollone *et al.*, Phys. Rev. Lett. **114**, 202501 (2015).
[102] S. Rothe, V. N. Fedosseev, T. Kron, B. A. Marsh, R. E. Rossel, and K. D. A. Wendt, Nucl. Instrum. Methods. B **317**, 561 (2013).